

# The Organization of Projections from Olfactory Glomeruli onto Higher-Order Neurons

## Highlights

- Lateral horn neurons (LHNs) divide into many distinctive morphology types
- Same-type LHNs have similar but non-identical glomerular connectivity
- Certain over-represented glomerular combinations wire onto multiple LHN types
- Over-represented combinations unite glomeruli co-activated by salient odor scenes

## Authors

James M. Jeanne, Mehmet Fişek,  
Rachel I. Wilson

## Correspondence

rachel\_wilson@hms.harvard.edu

## In Brief

Jeanne et al. use two-photon optogenetics to map connections from olfactory glomeruli onto lateral horn neurons in *Drosophila*. Certain combinations of glomeruli are over-represented. These are not similarly tuned glomeruli; rather, they are glomeruli whose co-activation signals a salient “odor scene.”

# The Organization of Projections from Olfactory Glomeruli onto Higher-Order Neurons

James M. Jeanne,<sup>1,2,3</sup> Mehmet Fişek,<sup>1,2,4</sup> and Rachel I. Wilson<sup>1,5,\*</sup>

<sup>1</sup>Department of Neurobiology, Harvard Medical School, 220 Longwood Avenue, Boston, MA 02115, USA

<sup>2</sup>These authors contributed equally

<sup>3</sup>Present address: Department of Neuroscience, Yale University School of Medicine, 333 Cedar Street, New Haven, CT 06510, USA

<sup>4</sup>Present address: Wolfson Institute for Biomedical Research and Department of Neuroscience, Physiology and Pharmacology, University College London, London, UK

<sup>5</sup>Lead Contact

\*Correspondence: [rachel\\_wilson@hms.harvard.edu](mailto:rachel_wilson@hms.harvard.edu)

<https://doi.org/10.1016/j.neuron.2018.05.011>

## SUMMARY

Each odorant receptor corresponds to a unique glomerulus in the brain. Projections from different glomeruli then converge in higher brain regions, but we do not understand the logic governing which glomeruli converge and which do not. Here, we use two-photon optogenetics to map glomerular connections onto neurons in the lateral horn, the region of the *Drosophila* brain that receives the majority of olfactory projections. We identify 39 morphological types of lateral horn neurons (LHNs) and show that different types receive input from different combinations of glomeruli. We find that different LHN types do not have independent inputs; rather, certain combinations of glomeruli converge onto many of the same LHNs and so are over-represented. Notably, many over-represented combinations are composed of glomeruli that prefer chemically dissimilar ligands whose co-occurrence indicates a behaviorally relevant “odor scene.” The pattern of glomerulus-LHN connections thus represents a prediction of what ligand combinations will be most salient.

## INTRODUCTION

The dimensionality of olfactory stimuli is intrinsically high. In other words, many parameters are needed to fully account for the physicochemical differences between odor molecules (Cleland, 2014; Haddad et al., 2008). Accordingly, a large number of unique odorant receptor proteins are devoted to the problem of odor discrimination. In the mouse, there are ~1,000 odorant receptors, with each glomerulus devoted to one receptor. An odor typically activates multiple glomeruli (Su et al., 2009), and these patterns of activity are detected by higher brain regions, where individual neurons pool input from multiple glomeruli (Apicella et al., 2010; Davison and Ehlers, 2011; Ghosh et al., 2011; Miyamichi et al., 2011; Sosulski et al., 2011). However, to sample all combinations of glomeruli would require a prohibitively large

number of neurons. We do not know which combinations are actually sampled, or why. In *Drosophila melanogaster*, there are only 50 glomeruli, but the brain still lacks the number of cells that would be required to represent more than a small fraction of all possible glomerular combinations. In short, the brain cannot exhaustively process its own “combinatorial code” for odors (Malnic et al., 1999).

How does the brain cope with the “curse of dimensionality” in olfaction? One strategy could be to sample in an unbiased fashion from all possible combinations of glomeruli (unbiased sampling). A different strategy would be to over-represent certain combinations of glomeruli that are predicted to be useful (predictive sampling). For example, the brain might sample combinations of glomeruli that prefer similar ligands. Alternatively, the brain might sample combinations of glomeruli whose co-activation is behaviorally salient, even if those glomeruli prefer chemically dissimilar ligands.

In *Drosophila*, two brain regions receive direct projections from olfactory glomeruli, the mushroom body and the lateral horn. Both are targeted by the axons of olfactory projection neurons (PNs). A typical PN is postsynaptic to just one glomerulus. Thus, the glomerular combination sampled by each postsynaptic cell is determined by the set of PNs that converge onto it. In the mushroom body, the cells that are postsynaptic to PNs (Kenyon cells) adopt the strategy of unbiased sampling: there is no widespread trend for certain combinations of glomeruli to be over-represented at the level of PN → Kenyon cell connections (Caron et al., 2013; Eichler et al., 2017). Although there is some evidence for limited bias in PN → Kenyon cell connections (Eichler et al., 2017; Gruntman and Turner, 2013; Tanaka et al., 2004; Zheng et al., 2017), it seems that unbiased sampling is the general rule. This wiring pattern implies that the overall strategy in the mushroom body is to maximize the diversity of odor representations (Litwin-Kumar et al., 2017).

The lateral horn is the other region that receives direct input from olfactory glomeruli. However, little is known about the connectivity from PNs onto lateral horn neurons (LHNs). The only clear rule is that LHNs with similar morphologies have similar connections (Dolan et al., 2017; Fişek and Wilson, 2014; Jeanne and Wilson, 2015; Kohl et al., 2013; Ruta et al., 2010). Based on anatomy alone, several studies have ventured predictions about which combinations of PNs might converge onto LHNs (Ebrahim

et al., 2015; Grosjean et al., 2011; Jefferis et al., 2007; Min et al., 2013; Ronderos et al., 2014; Silbering et al., 2011), but these predictions are largely untested. Thus, the wiring diagram from PNs to LHNs remains essentially unmapped. We do not know whether certain combinations of glomeruli are over-represented—and if so, what olfactory features these over-represented combinations might signal.

The lateral horn has been suggested to be analogous to the vertebrate amygdala, which receives a major projection from the olfactory bulb (Luo et al., 2010; Miyamichi et al., 2011; Sosulski et al., 2011). However, the wiring from glomeruli onto amygdala neurons is no better understood than the wiring of the lateral horn. The gaps in our knowledge of these higher olfactory brain regions have led to the suggestion that there are perhaps no intermediate levels of complexity in the wiring of the olfactory system (Fairhall, 2014)—e.g., no repeated motifs built from specific combinations of glomeruli. If this is true, then the olfactory system is radically different from the visual system, which contains a hierarchy of increasingly complex feature-detection cells. Visual feature-detection cells are built from specific combinations of inputs: for example, some cells detect visual edges because they pool inputs from cells with co-linear receptive fields. Are there no analogous repeated circuit motifs in the olfactory system that are built from specific combinations of glomeruli?

To address this question, we developed a method to map long-range functional connections from olfactory glomeruli to LHNs on a large scale, at cellular resolution. We find that certain combinations of glomeruli are over-represented, and these combinations are not generally comprised of glomeruli that are co-activated by the same ligands; instead, they are glomeruli whose co-activation defines an ecologically salient odor scene. These over-represented combinations represent a prediction of what combinations of ligands will be meaningful to the organism. This predictive sampling strategy exists in parallel with the unbiased sampling strategy of the mushroom body. The curse of dimensionality is a general problem in neural computation—with applications in visual object recognition, for example. Our results show that, rather than implementing one strategic solution to the “curse,” the brain implements two strategies simultaneously.

## RESULTS

### Glomerular Photostimulation Is Specific and Reliable

Our approach to mapping connectivity was to optogenetically stimulate PNs in single glomeruli while making whole-cell recordings from individual LHNs. To render PNs photosensitive, we expressed the channelrhodopsin variant ReaChR (Inagaki et al., 2014; Lin et al., 2013) under the control of the PN driver line *GH146-Gal4* (Stocker et al., 1997). This Gal4 line drives expression in PNs in 39 of the 50 olfactory glomeruli. We removed the brain from the head, and we used 2-photon excitation to photostimulate PN dendrites in each glomerulus. We divided the antennal lobe volume into 13 optical slices, and each slice into a grid of  $7 \times 7 \mu\text{m}$  fields. Each field was raster-scanned, and fields were visited in a random sequence. The volume of effective photostimulation extended  $8 \mu\text{m}$  in the z-dimension, and so each square defines a  $7 \times 7 \times 8 \mu\text{m}$  voxel (STAR Methods), which is

smaller than a glomerulus. At the end of each experiment, we bath-applied a vital dye, allowing us to outline the boundary of each glomerulus and thereby assign voxels to glomeruli.

The usefulness of this method depends on (1) how reliably it evokes spikes in the PNs inside the stimulated glomerulus, and (2) whether PN spiking responses are specifically restricted to that glomerulus. To check these outcomes, we performed whole-cell recordings from PNs (Figure 1A), and we filled the recorded PN with dye to identify the glomerulus innervated by its dendrites (the home glomerulus). We observed that PNs essentially never spiked in this *ex vivo* preparation in the absence of photostimulation, but they did spike when photostimulated (Figure 1B). We almost always observed a PN spiking response to at least two voxels in the home glomerulus (Figures 1B–1F and S1). We occasionally observed spiking when we stimulated a voxel outside the home glomerulus, but these off-target voxels were typically spatially isolated, or else represented obvious “bleed through” from the home glomerulus into the edge of a neighboring glomerulus. We therefore defined a hit as a glomerulus that contained at least 2 adjacent positive voxels (spike-evoking voxels), with positive voxels comprising at least 25% of the glomerulus, and also covering the center of the glomerulus (Figure S2). Importantly, we used identical criteria for defining glomerular hits in PN recordings and in subsequent LHN recordings.

Given these criteria, reliability was good (the correct hit rate was high), and specificity was also good (the false hit rate was almost zero) (Figure 1G). This means we can use this method to reliably and specifically stimulate PNs in single glomeruli. In particular, photostimulation does not recruit much polysynaptic excitation within the antennal lobe; otherwise the false hit rate would be higher. Note that we are using an *ex vivo* preparation where overall activity is lower than normal, which likely explains why polysynaptic circuits are evidently not recruited.

### LHN Responses to Glomerular Stimulation Are Consistent with Direct Connections

Next, we performed whole-cell recordings from many LHNs while photostimulating PNs (Figure 2A), using diverse Gal4 lines to target a broad sample of LHNs (STAR Methods). In a typical recording, we saw responses to only a few voxels (Figures 2B, 2C, and S3). LHN responses were stable over the course of an experiment (Figure S4). In each recording, we scored glomeruli as “hits” using the same criteria described above.

LHN responses were almost all excitatory, and this is what one would expect from direct PN → LHN connections, because most *GH146*<sup>+</sup> PNs are cholinergic. Inhibitory responses were occasionally observed when stimulating glomerulus DA1 or VA1v (Figure 2D). Notably, these are the only two glomeruli that contain *GH146*-positive GABAergic PNs in addition to *GH146*-positive cholinergic PNs (Jefferis et al., 2007; Lai et al., 2008; Marin et al., 2002; Wong et al., 2002) (Figure S5). Thus, all the inhibition we observed in LHNs is likely due to monosynaptic connections from GABAergic PNs.

In principle, some responses might reflect polysynaptic input to LHNs (either excitatory or inhibitory). However, recruitment of these circuits would presumably require spiking in LHNs, and we observed spikes in only a minority of LHN responses

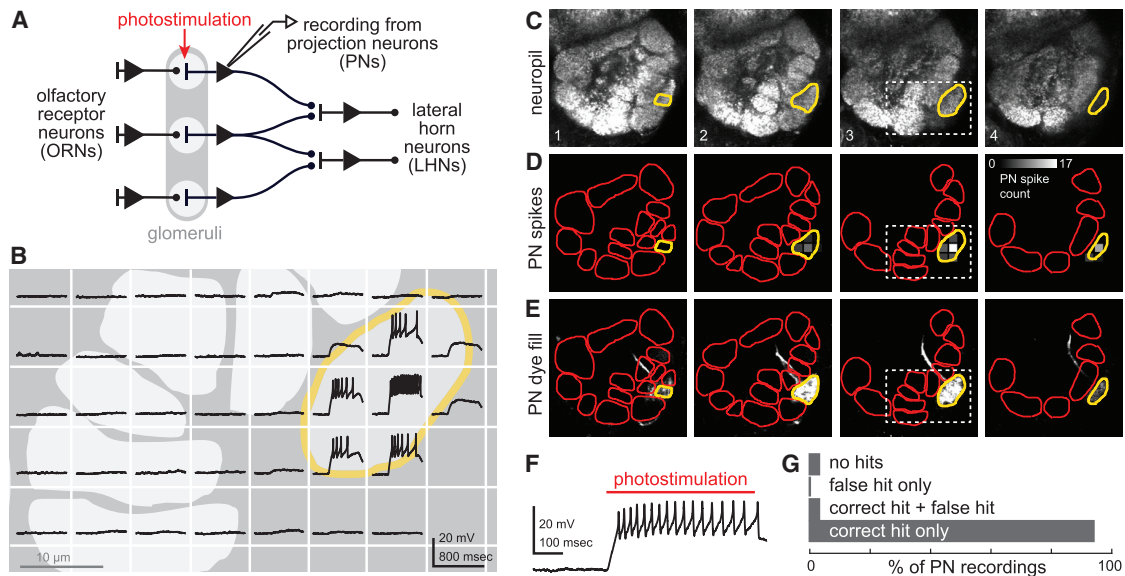


**Figure 1. Glomerular Photostimulation Is Specific and Reliable**

(A) Recording from ReaChR-expressing PNs in the antennal lobe.  
 (B) PN responses to stimulation, shown within the corresponding voxel, with glomeruli in pale gray. Voxels that evoked spiking were confined to the home glomerulus (yellow).  
 (C) Four optical slices through the antennal lobe (each 6  $\mu$ m apart), numbered from anterior to posterior, showing neuropil stain. In total, 11–13 slices were imaged per experiment. Dashed line encloses the enlarged area in (B).  
 (D) PN spiking responses (grayscale) for each of these slices. See [Figure S1](#) for the full map for this PN.  
 (E) The same slices, now imaged at a wavelength that allows visualization of the dye in the PN. Note that the home glomerulus of this PN is the glomerulus that evoked spiking, meaning a correct hit.  
 (F) PN voltage response to photostimulation. See [Table S1](#) for PN firing rates.  
 (G) PN recordings by outcome ( $n = 33$  PNs, each recorded in a different brain). A false hit is a glomerulus that does not contain the PN's dendrites, but that nonetheless fulfills the criteria for a hit. See also [Figure S2](#).

(0.8% of voxels overall, and 20.2% of voxels with a significant response). Thus, most of the connections we observed are probably direct PN  $\rightarrow$  LHN connections. The possibility that some connections may be indirect is a limitation of our approach.

### Single-PN Glomeruli and Multi-PN Glomeruli form Equally Strong Connections onto LHNs

We found that some excitatory responses consisted of regularly spaced excitatory postsynaptic potentials (EPSPs) ([Figure 2E](#)). These were typically cases where the photostimulated glomerulus contains a single PN ([Grabe et al., 2016](#)). By contrast, other excitatory responses consisted of irregularly spaced EPSPs, or else graded depolarizations ([Figure 2F](#)). These were typically cases where the photostimulated glomerulus contains multiple sister PNs. Sister PNs converge in the lateral horn ([Jeanne and Wilson, 2015; Kazama and Wilson, 2009; Marin et al., 2002; Wong et al., 2002](#)), and we would expect that stimulating sister PNs would elicit EPSPs that overlap at irregular intervals.

As a point of comparison, we also recorded from mushroom body Kenyon cells. A Kenyon cell typically receives input from at most one PN in a given glomerulus ([Caron et al., 2013](#)). As expected, we found that every Kenyon cell response consisted of regularly spaced EPSPs ([Figure S5](#)). This further supports the idea that regularly spaced EPSPs indicate input from a single PN.

Interestingly, we found that LHN responses were no stronger for multi-PN glomeruli than for single-PN glomeruli ([Figure 2G](#)). This suggests there is a compensatory process that adjusts the strength of unitary PN  $\rightarrow$  LHN connections for the number of convergent PNs. This would explain why the total strength of a glomerular connection does not depend on how many PNs the glomerulus contains.

### Olfactory Inputs to LHNs Are Sparse and Over-represent Certain Glomeruli

Across a total sample of 110 LHNs, we found that the average glomerulus made connections with 13% of our LHN sample. Conversely, the average LHN received input from 4.8 glomeruli. However, because we were stimulating excitatory PNs in only 39 of 50 glomeruli, we predict that the average LHN actually receives excitatory input from 6.2 glomeruli. There was a wide variation across LHNs in the number of connected glomeruli ([Figure 2H](#)).

Across all LHNs, we found responses to photostimulation for 37 of the 39 *GH146*<sup>+</sup> glomeruli. Some glomeruli made a disproportionately large number of connections, particularly VA1d, VA1v, DC3, and VA6 ([Figure 2I](#)). Interestingly, all these glomeruli are narrowly tuned to odors ([Dweck et al., 2015; Hallem and Carlson, 2006; Lin et al., 2016; Ronderos et al., 2014; van der Goes van Naters and Carlson, 2007](#)).

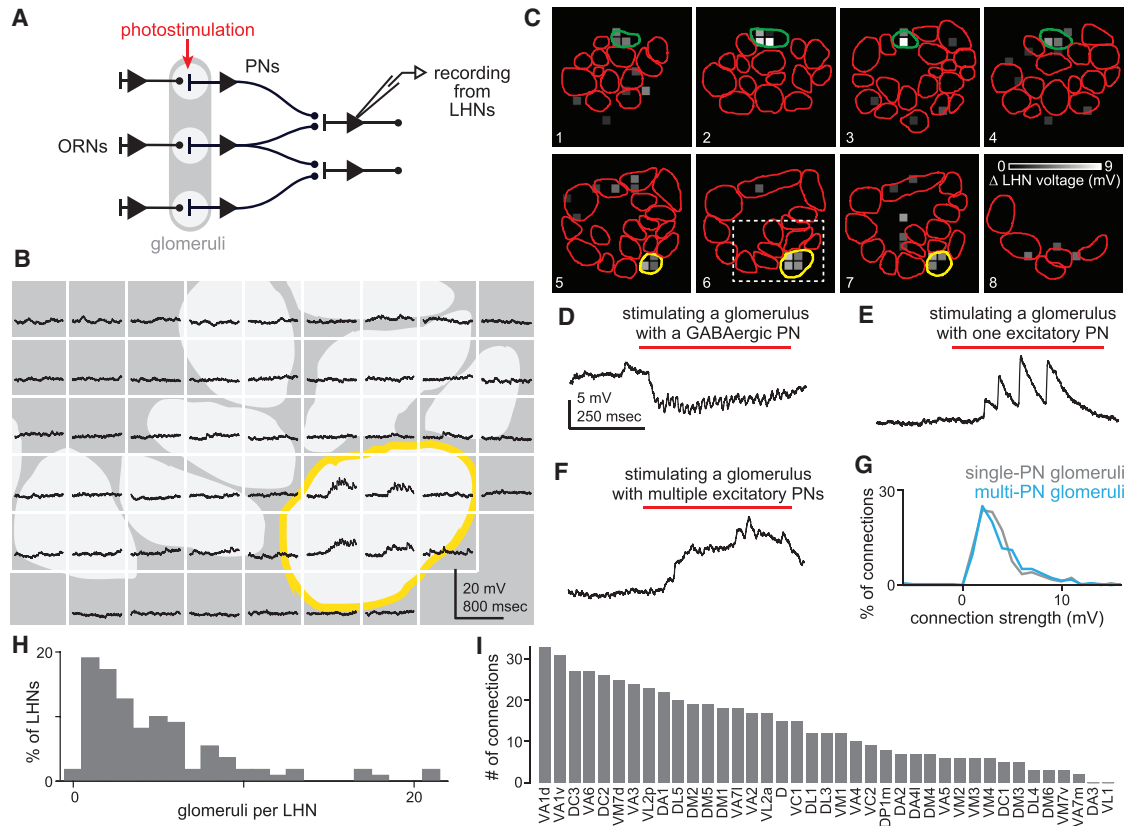


**Figure 2. LHN Responses to Photostimulation Are Sparse and Equally Strong for Single- and Multi-PN Glomeruli**

(A) Recording from LHNs.  
 (B) Responses of this LHN to stimulation of 50 voxels. One glomerulus was a hit (yellow). See also Figure S4.  
 (C) Eight optical slices (each 6  $\mu\text{m}$  apart), numbered from anterior to posterior. Grayscale values represent LHN voltage responses. Two hits are shown (green and yellow). Dashed line encloses the enlarged area in (B). See also Figures S2 and S3.  
 (D) Inhibitory postsynaptic potentials (IPSPs) evoked by photostimulation. See also Figure S5.  
 (E) Stimulation of a single-PN glomerulus typically evokes large EPSPs at regular intervals.  
 (F) Stimulation of multi-PN glomerulus typically evokes graded or irregular responses.  
 (G) Connection weight histograms. On average, single-PN weights ( $3.8 \pm 0.2$  mV) and multi-PN weights ( $4.0 \pm 0.1$  mV) are not significantly different ( $p = 0.42$ , Wilcoxon rank-sum test).  
 (H) Histogram of glomerular hits per LHN ( $n = 110$  LHNs, each recorded in a different brain).  
 (I) Number of connections detected per glomerulus, across all 110 LHN recordings.

### Automatically Classifying LHNs by Morphology

Before analyzing our connectivity data in depth, we considered the notion of “LHN types.” LHNs are morphologically diverse (Figure 3A), and LHNs with similar morphologies have similar odor tuning (Figure 3B). LHNs with similar morphologies (and odor responses) also seem to receive similar connections from olfactory glomeruli, although connectivity data are limited (Dolan et al., 2017; Fişek and Wilson, 2014; Jeanne and Wilson, 2015; Jefferis et al., 2007; Kohl et al., 2013; Ruta et al., 2010; Tanaka et al., 2004). These observations motivated us to classify LHNs into morphology types.

Our goal was to make LHN classification automatic. First, we collected both morphology data and odor-response data from several groups of LHNs (Figures 3A and 3B). We filled each recorded cell with dye, traced its skeleton, registered it to a template brain, and used the NBLAST algorithm to measure similarity between morphologies (Costa et al., 2016). We

then hierarchically clustered cells based on their morphological similarity (Figure 3C). We defined a threshold that cut morphological clusters as finely as possible, while also keeping LHNs with similar odor tuning in the same cluster (Figure 3D); this threshold was an NBLAST linkage distance of 0.65. This yielded a classification system where odor-tuning dissimilarity was significantly lower within a morphology type than between morphology types (Figure 3E).

We then applied this same method to our full dataset of LHN morphologies. Using the same threshold as before, we classified a total of 110 LHNs into 39 morphology types (Figures 4A, 4B, and STAR Methods). There are  $\sim 250$  LHN morphology types in all (Frechter et al., 2018), but because the cells in our sample collectively arborize throughout the lateral horn (Figure S6B), they likely capture much of the diversity in the full LHN cohort.

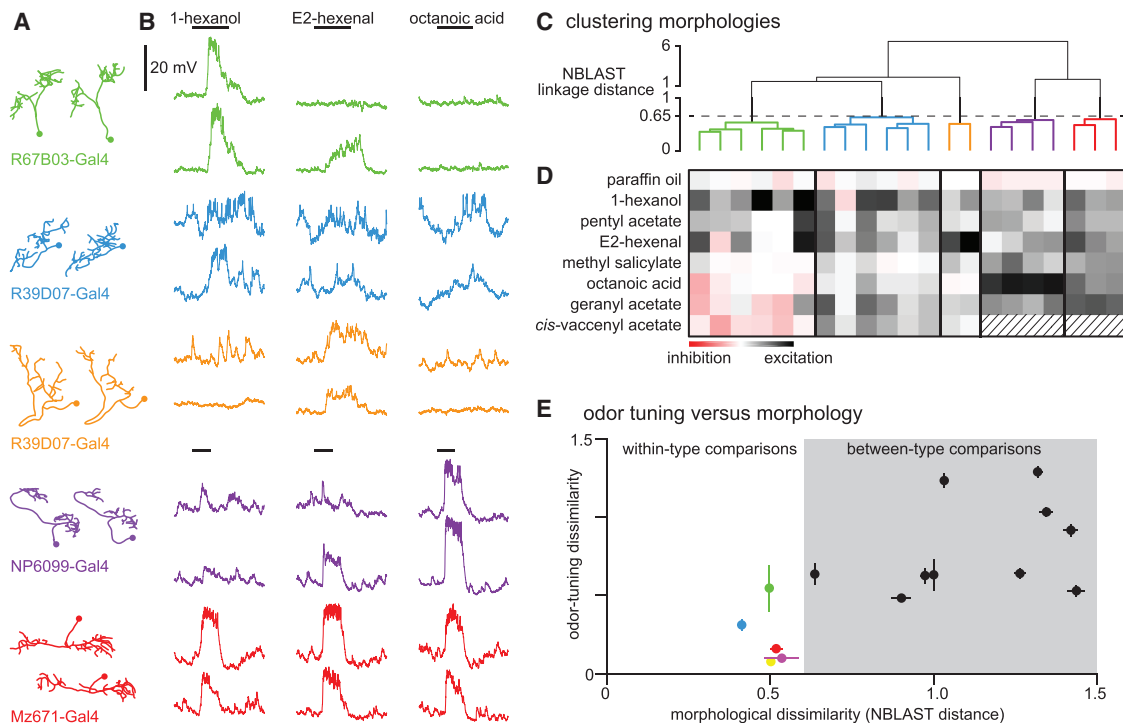


**Figure 3. Dividing LHNs into Morphology Types**

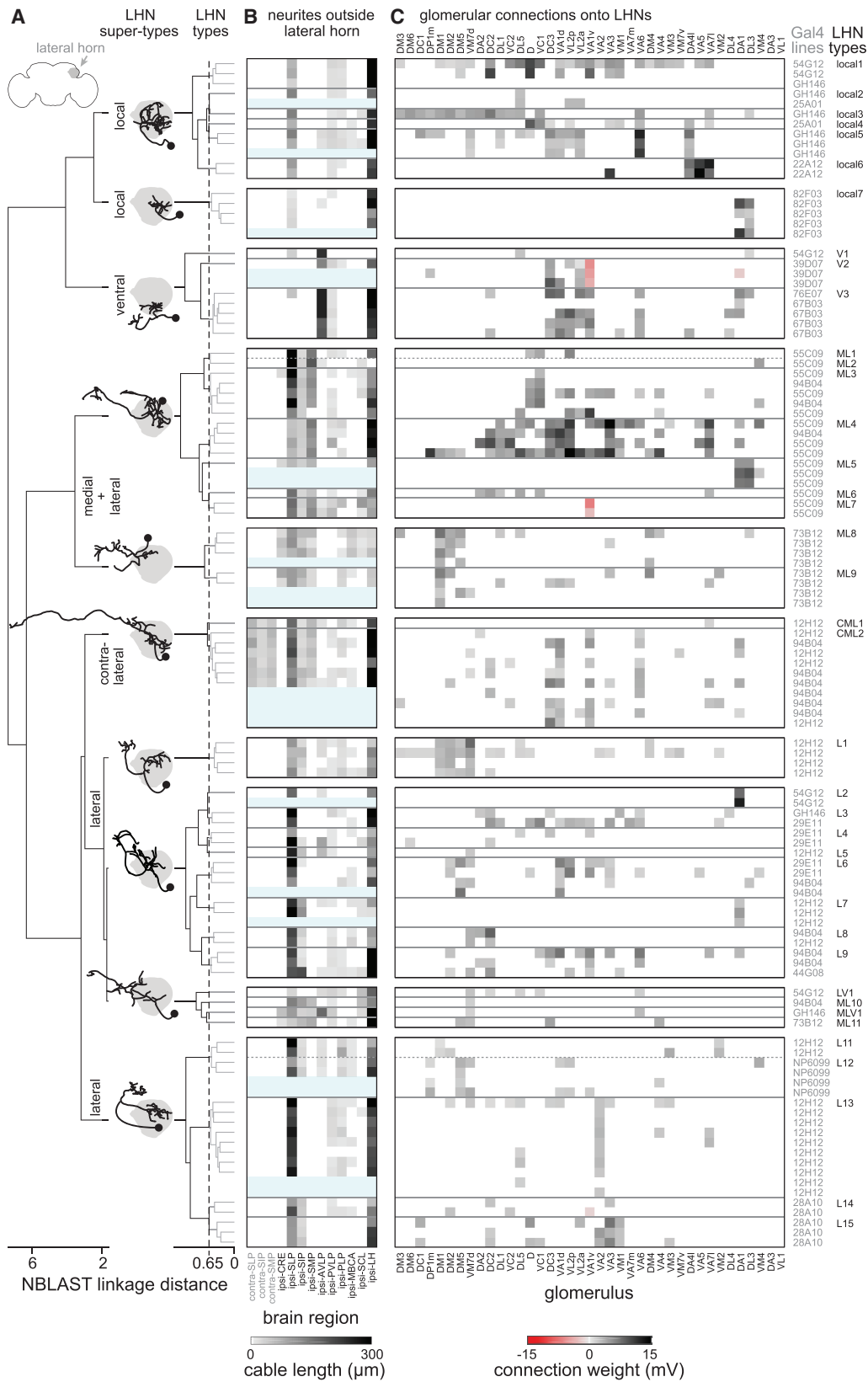
(A) Ten sample LHN morphologies traced from dye-fills. Note that these cells divide into types. We added somata to these images because somata were detached when the pipette was removed; in some cases, we also added a short segment of neurite directly attached to the soma, for the same reason. (B) For each morphology type, example responses of 2 cells to 3 odors. Odor stimulus duration was 1 s (top 6 rows) or 0.5 s (bottom 4 rows). Morphology and odor data were collected in the same experiments (top 6 rows) or separate experiments (bottom 4 rows). (C) Morphologies were hierarchically clustered on NBLAST linkage distances and then divided into types (horizontal dashed line). Colors match (A) and (B). Each cell was recorded in a different brain. (D) Corresponding odor responses for the same cells, measured as the mean change in voltage during the stimulus. Hatching means odor not tested. The color scale ranges from  $-10$  to  $+10$  mV, with a few off-scale excitatory responses cropped to the maximum; the scale is  $-30$  to  $+30$  mV for *NP6099* and *Mz671*. (E) Odor tuning dissimilarity (LHN-LHN odor correlation distance) versus morphological dissimilarity (NBLAST distance), averaged across all the cell pairs for a given comparison,  $\pm$ SEM. This yields 15 values, i.e., 5 within-type comparisons and 10 (5 choose 2) different-type comparisons. Odor-tuning dissimilarity is significantly higher across types than within a type ( $p = 0.002$ ,  $t$  test). If we ignore type boundaries and simply regress odor-tuning dissimilarity against morphological dissimilarity, we find a strong and significant relationship ( $r = 0.71$ ,  $p = 0.003$ ,  $n = 15$  cell-pair averages). Within-type comparison points match colors in (A)–(C).

### LHNs Belonging to the Same Morphology Type Have Similar but Non-identical Connectivity

We next considered the connectivity of our full LHN data set (110 LHNs), now taking LHN morphology types into account. We found that LHNs belonging to the same morphology type generally had similar connectivity (Figure 4C). However, their connectivity was rarely identical. Overall, the mean pairwise connectivity correlation for same-type LHNs was only  $\sim 0.6$  (Figure 5A). This may seem surprisingly low. To put this number in perspective, we reanalyzed a sample of 38 paired PN-LHN recordings reported in a previous study (Fişek and Wilson, 2014); this study reported two aberrations (one absent connection that was typically present, plus one aberrant connection that was typically absent), which implies a biological “error rate” of  $\sim 5\%$  (2/38). To estimate the effect of a 5% biological “error rate,” we simulated a set of typical LHNs as receiving binary input from 5 of 39 glomeruli, and we randomly flipped the sign of 5% of connections in each cell; this showed that simulated LHNs of the same type are ex-

pected to have within-type correlations of  $\sim 0.7$  (Figure 5A). Of course, biological “errors” in connectivity might not be errors at all; they might be adaptive individual variations. The key point here is that even a seemingly low rate of biological connectivity variation (5% per glomerulus-LHN pair) will produce a considerable net divergence between cells belonging to the same LHN type, simply because the number of glomeruli is so large.

In addition, some apparent differences between same-type LHNs are likely due to experimental error. Given the data in Figure 1F, we estimate that we failed to stimulate a targeted PN 3% of the time; conversely, we stimulated the wrong PN 0.2% of the time (false hits and false misses computed per glomerulus). We may have also failed to accurately detect some LHN responses, even when PNs were correctly stimulated. However, experimental error is unlikely to be the dominant factor here, because documented biological per-glomerulus variation is large enough to account for most of the divergence we observed between same-type LHNs.



(legend on next page)

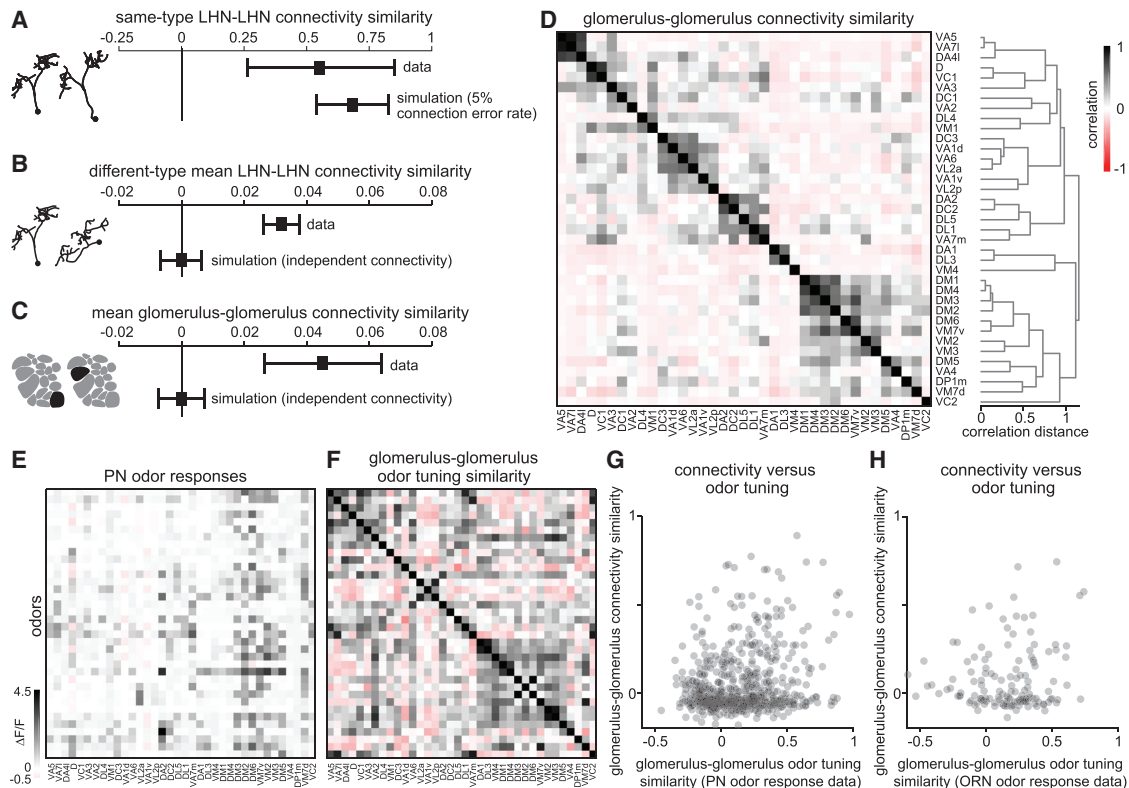


**Figure 5. Connectivity Similarity between Cells and between Glomeruli**

(A) Top: pairwise correlations between the connectivity of same-type LHNs (mean  $\pm$  SD across 95 pairs). Bottom: correlations are similar when we simulate a set of LHNs that initially receive binary input from 5 of 39 glomeruli (so all LHNs are identical) and then randomly flip 5% of connections. (In Figures 5, 6, and 7B, we omitted the 3 LHN types with particularly broad connectivity, namely, local1, local3, and ML4; see STAR Methods).

(B) Top: mean pairwise correlations between different-type LHNs (mean  $\pm$  SD, 1 sampled LHN per type, 5,000 resamples). Bottom: the connections of different-type LHN pairs were independently permuted, to simulate a situation where each LHN type receives independent inputs. This produced a mean correlation of 0, and a significant difference from the measured correlations of different-type LHN pairs ( $p = 8 \times 10^{-4}$ , bootstrap resampling test, 5,000 resamples).

(C) Top: mean pairwise correlation between glomeruli (mean  $\pm$  SD, 1 sampled LHN per type, 5,000 resamples). Bottom: the LHN types targeted by each glomerulus were independently permuted, to simulate a situation where each glomerulus targets an independent set of LHN types ( $p = 0.0024$ , bootstrap resampling test).

(D) All pairwise correlations between glomeruli (again with one sampled LHN per type, mean  $\pm$  SD, 5,000 resamples, omitting glomeruli with no connections in our dataset). Glomeruli were then clustered on the basis of these correlations (dendrogram at right).

(E) PN odor responses from [Badel et al. \(2016\)](#).

(F) Glomerulus-glomerulus similarity in odor tuning, from data in (E). Color scale as in (D).

(G) Similarity in connectivity versus similarity in odor tuning ( $r = 0.20$ ,  $p = 5 \times 10^{-7}$ ).

(H) Same as (G) but using olfactory receptor neuron odor responses from [Hallem and Carlson \(2006\)](#). Here, the correlation falls short of significance ( $r = 0.14$ ,  $p = 0.11$ ).

### Different LHN Types Receive Input from Non-independent Glomerular Combinations

In the mushroom body, each Kenyon cell has a nearly independent set of input glomeruli ([Caron et al., 2013](#); [Eichler et al., 2017](#)). In other words, if we pick a typical Kenyon cell at random,

and we find that it receives input from glomerulus A, then we have almost no ability to predict whether it also receives input from glomerulus B, C, etc. How does this compare to the lateral horn? We have already seen that same-type LHNs have similar inputs ([Figure 5A](#)). By contrast, we might hypothesize that

**Figure 4. Glomerular Connectivity onto a Large and Diverse Set of LHN Morphology Types**

(A) LHNs were clustered into 39 morphology types. Ten example types are shown here, one for each broad class of types (“super-types”). See [Figure S6](#) for examples of each type and [Data S1](#) for all morphologies.

(B) Length of each cell’s neurites outside the lateral horn, per brain region. See [STAR Methods](#) for abbreviations. Blue shading denotes LHNs with incomplete morphology data due to failed template registration ( $n = 5$ ), dim dye-fill ( $n = 6$ ), or no dye-fill ( $n = 10$ ). We manually assigned these 21 LHNs to a morphology type using partial morphology data (if available) or connectivity data (if not).

(C) LHN voltage responses to stimulation of each glomerulus. LHNs are grouped by morphology type (solid horizontal lines). Two type divisions were drawn manually (dashed horizontal lines). Gal4 lines and type names are listed at right. Data are available in [Table S2](#).

different-type LHNs have independent inputs. This would be an efficient way to represent as many glomerular combinations as possible.

Contrary to this hypothesis, we found that inputs to different LHN types were not independent. We sampled a random cell from every LHN type, and we computed pairwise correlations between all LHNs. With many resamples, we found a positive mean correlation between different-type LHNs (Figure 5B). If LHNs were independent, the mean correlation would be zero; we can simulate this by taking all our different-type LHN pairs, independently permuting the glomerular inputs onto each cell, and then recomputing the correlations (Figure 5B). We found a significantly higher correlation in the data than in the simulated case of independent connectivity. In short, these analyses demonstrate that different LHN types represent non-independent glomerular combinations.

We also considered the same issue from the perspective of glomeruli, rather than LHN types. Again, we sampled a random cell from every LHN type, and we computed pairwise correlations between all glomeruli. Mean correlations across glomeruli were consistently positive, and significantly different from the permuted case (Figure 5C). This shows that different glomeruli target non-independent sets of LHN types.

To visualize relationships among glomeruli, we computed a glomerulus-glomerulus correlation matrix (Figure 5D). When sorted by similarity, this matrix exhibited a rough block-diagonal structure, with each block defining a group of related glomeruli with similar connectivity. Some high correlation values were found far off the diagonal, indicating that the corresponding glomeruli participate in multiple combinations.

### Glomeruli with Similar Connection Patterns Share Weakly Similar Chemical Tuning

Do glomeruli targeting similar LHN types share similar chemical tuning? To address this question, we compared our connectivity data to a published set of PN odor responses obtained from calcium imaging experiments (Badel et al., 2016). This odor response dataset (Figure 5E) is a useful point of comparison because it focuses on the same PNs that we photostimulated. For all pairs of glomeruli, we regressed similarity in connectivity (Figure 5D) against similarity in odor tuning (Figure 5F). We found a relationship that was statistically significant but weak ( $r = 0.20$ ,  $p = 5.0 \times 10^{-7}$ , Figure 5G).

We then repeated this analysis with another odor tuning dataset, this time obtained from olfactory receptor neuron electrophysiological recordings (Hallem and Carlson, 2006). Here, we found a similarly weak correlation between connectivity and tuning ( $r = 0.14$ ), which did not reach statistical significance ( $p = 0.11$ , Figure 5H). The Hallem dataset comprises more odor stimuli, but there are fewer glomeruli in this dataset that overlap with the glomeruli in our study (17 glomeruli versus 37 in the Badel dataset), meaning many fewer glomerulus-glomerulus combinations (136 versus 666) and thus less statistical power.

These analyses indicate that there is a small bias (at most) for glomeruli with similar chemical tuning to target similar LHN types. However, many pairs of glomeruli that make similar connections have dissimilar odor tuning. This motivated us to look more closely at the odor tuning preferences of the glomeruli with the most similar connections.

### Convergent Glomeruli Define Salient “Odor Scenes”

Next, we asked which pairs of glomeruli converge significantly more than expected. For each glomerular pair, we counted the number of individual LHNs in our dataset that received convergent input from that pair. We then used a permutation test to identify which pairs of glomeruli were statistically significant, with a false discovery rate set to 5% (this corrects for the fact that we are conducting multiple comparisons; STAR Methods). This procedure identified 21 significant pairs (Figure 6A). This analysis treats all LHNs as independent samples; it identifies the glomeruli that converge frequently onto same-type LHNs or different-type LHNs. We found that some paired glomeruli were similarly tuned, while many others were not (Figure 6B).

Glomerulus DA1 and DL3 formed one significant pair (Figure 6C). These glomeruli are both selective for cis-vaccenyl acetate (Ejima et al., 2007; Ha and Smith, 2006; Kurtovic et al., 2007; Lebreton et al., 2014; Liu et al., 2011; van der Goes van Naters and Carlson, 2007; but see Dweck et al., 2015; Pitts et al., 2016). This odor is a male pheromone. In females, like our experimental animals, it promotes aggregation and mating (Kurtovic et al., 2007; Lebreton et al., 2014; Liu et al., 2011; Schlieff and Wilson, 2007), whereas in males it promotes aggression (Wang and Anderson, 2010). Thus, the LHNs that combine input from DA1 and DL3 are likely to participate in social behaviors.

We found many significant pairs associated with esters or alcohols (Figure 6D, top) (VM7d, DM5, DM1, DM4, DM2, VA3, D; de Bruyne et al., 1999, 2001; Hallem and Carlson, 2006; Kreher et al., 2005; Münch and Galizia, 2016). These are fruit volatiles (El Hadi et al., 2013; Zhang and Chen, 2014) that are also produced by the yeasts that *Drosophila* eat (Antonelli et al., 1999; Becher et al., 2012; Christiaens et al., 2014; Scheidler et al., 2015; Tsakiris et al., 2010). Some pairs comprise glomeruli with similar tuning (e.g., DM1–DM4). Other pairs comprise glomeruli whose preferred ligands are chemically dissimilar, although they originate from similar sources (e.g., DM2–VA3). The LHNs that combine input from these glomeruli may play roles in food seeking or feeding. Interestingly, glomerulus DM1 provides strong input to many of these LHNs, and this glomerulus potently elicits upwind walking (Bell and Wilson, 2016).

Moreover, we found another group of significant pairs associated with terpenoid odors (Figure 6D, bottom). This includes VC1 (fenchone; Goldman et al., 2005) and DC1 (valencene, limonene, linalyl acetate; Dweck et al., 2013; Hallem and Carlson, 2006), as well as glomerulus D, which is the best receptor for several terpenoids ( $\alpha$ -terpineol, linalool; Münch and Galizia, 2016). These terpenoids are produced by plants and yeast (Carrau et al., 2005; Dugelay et al., 1992; Surburg and Panten, 2006), and they inhibit the growth of bacteria that are pathogenic to *Drosophila* (Carson et al., 2002; Kazemi et al., 2012; Soković et al., 2010). Moreover, limonene and valencene promote egg laying (Dweck et al., 2013), and terpenes can repel wasps that predate on immature *Drosophila* (Dweck et al., 2013). Thus, the LHNs that combine input from these glomeruli may guide females to egg-laying sites endowed with natural antibiotics and predator repellants.

Finally, we found one group of glomeruli whose members formed many significant pairs (Figure 6E). Two glomeruli in

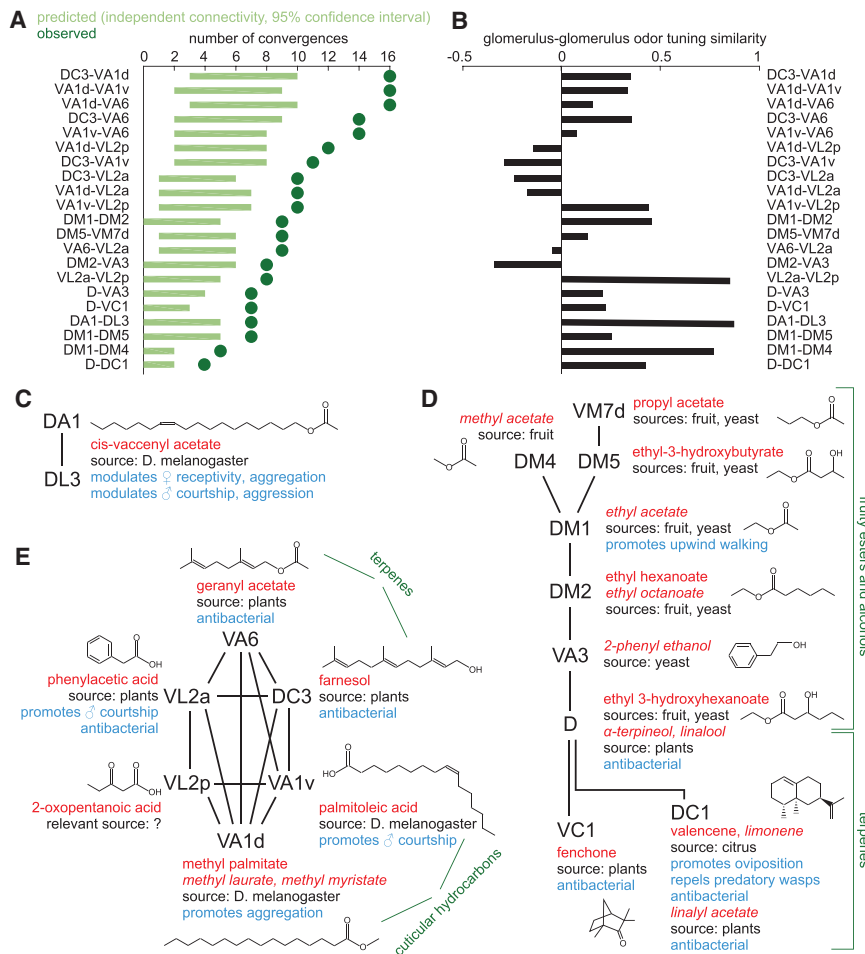


**Figure 6. Significant Glomerular Pairs Define Salient Odor Scenes**

(A) All statistically significant glomerular pairs. These pairs converge more often than we would predict (in a hypothetical scenario where all glomeruli made independent connections onto LHNs). Circles: observed number of convergences. Bars: predicted number (permutation test, 95% confidence interval).

(B) Odor-response correlations between the same glomerular pairs. Correlations are computed from the PN response data of *Badel et al. (2016)*. The exception is D-DC1, which is from the *Drosophila* Database of Odorant Responses (*Münch and Galizia, 2016*) because DC1 does not appear in the *Badel* dataset.

(C–E) Significant pairs and associated odors. Paired glomeruli are connected by lines. Listed is the best odor for each glomerulus (unitalicized) and/or an odor for which the glomerulus is the best responder (italicized). Chemical structures are for the first listed odor. See *Table S3* for references on natural sources relevant to *D. melanogaster* (black annotations) and behavior or ecology (blue).

the lateral horn (*Ebrahim et al., 2015; Grosjean et al., 2011; Jefferis et al., 2007; Min et al., 2013; Ronderos et al., 2014; Silbering et al., 2011*). These predictions are based on pooling PN morphologies from different brains and registering them to a standard template brain. To evaluate these predictions retrospectively, we examined the data collected by these previous studies; we found that some functionally convergent PNs have highly overlapping

this group, VA1d and VA1v, respond selectively to fly odors that promote aggregation and courtship (*Dweck et al., 2015; Lin et al., 2016; van der Goes van Naters and Carlson, 2007*). Three other glomeruli in this group respond best to plant odors (*Surburg and Panten, 2006*); these glomeruli are DC3 (farnesol; *Ronderos et al., 2014*), VA6 (geranyl acetate; *de Bruyne et al., 2001; Hallem and Carlson, 2006*), and VL2a (phenylacetic acid; *Grosjean et al., 2011*). Phenylacetic acid promotes courtship (*Grosjean et al., 2011*), while phenylacetic acid, farnesol, and geranyl acetate inhibit pathogenic bacteria (*Inoue et al., 2004; Kakarla and Ganjewala, 2009; Kim et al., 2004*). Thus, the LHNs that combine input from glomeruli in this group may drive mating and aggregation in food patches containing natural antibiotics.

In summary, the significant glomerular pairs we have identified define complex “odor scenes.” These odor scenes often combine chemically dissimilar volatiles. Different scenes are linked to different behaviors – e.g., mating, feeding, or egg laying.

### Comparing Actual Connectivity with Predicted Connectivity

Previous studies have predicted which glomeruli might wire together onto LHNs, based on which PN axons overlap in

axons, but others do not (*Figure 7A*). We then regressed similarity in PN axon morphology against similarity in PN→LHN connectivity, for all glomerular pairs; this showed a relationship that was statistically significant but weak (*Figure 7B*). Indeed, there are many unexpected functional convergences in our dataset, given previous predictions based on PN axon overlap. This situation is not illogical: two PN axons need not overlap at all in order to converge onto the same LHNs, since many LHNs have large arbors in the lateral horn (*Figures 4A and S6*).

Apposition of axons and dendrites is another potential predictor of lateral horn connectivity (*Jefferis et al., 2007*). We therefore measured appositions of PN axons and LHN dendrites. Specifically, we overlaid our LHN morphology data with the PN axon morphology data collected by previous studies (*Figure 7C*), all registered using a standard template brain; we then quantified the number of axon-dendrite appositions (*Stepanyants and Chklovskii, 2005*) within 1  $\mu\text{m}$ . We found that the probability of PN→LHN connectivity grew steadily with the number of axon-dendrite appositions (*Figure 7D*). However, the probability of connectivity reached an asymptote at about 0.3. Thus, even the most highly apposed axon-dendrite pairs were generally not connected.

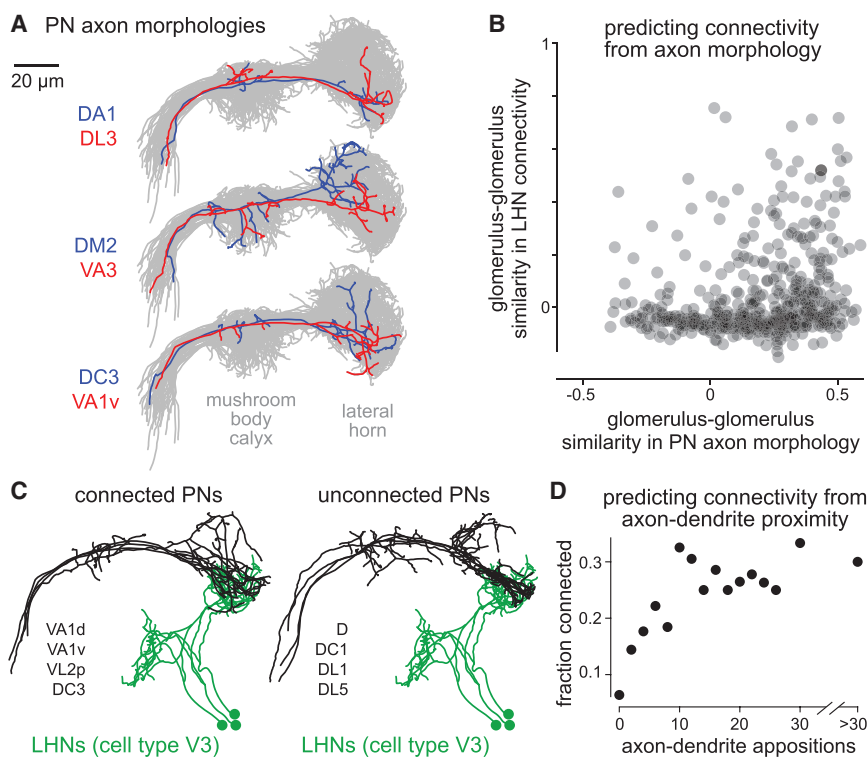


**Figure 7. Comparing Actual Connectivity with Predicted Connectivity**

(A) PN axons for three pairs of significantly converging glomeruli (from Figure 6A). (B) For all pairs of glomeruli, similarity in LHN connectivity is plotted versus similarity in PN axon morphology. There is a weak but significant correlation ( $r = 0.23$ ,  $p = 7 \times 10^{-7}$ ,  $n = 465$  pairs, corresponding to the 31 glomeruli that are common to the connectivity dataset and the PN morphology dataset). (C) Left: five individual V3 cells overlaid with axons from some PN types that were typically connected to these LHNs. Right: same LHNs, now overlaid with axons from some PN types that were never connected. (D) Fraction of PN-LHN pairs connected versus number of axon-dendrite appositions. PN-LHN pairs were binned by the number of appositions between them ( $n = 2,937$  pairs).

knew were unconnected (DM1 and DM2) that can be driven with selective odors (methyl acetate and ethyl hexanoate; Fişek and Wilson, 2014; Hallem and Carlson, 2006). All these glomerulus-LHN connections are summarized in Figure 8A.

It is important to realize that cell-cell proximity can be an excellent predictor of connectivity in the *Drosophila* nervous system: when the two cells in question are measured in the same individual, cell-cell proximity is strongly related to the number of synaptic connections between the two cells (Gerhard et al., 2017; Tobin et al., 2017). Uncertainty arises when pooling cells from different brains; here, proximity measurements are less precise, due to registration errors and brain-to-brain cell shape variations. Our results show that cell morphologies pooled across individuals have significant power to predict connectivity, but the accuracy of this sort of prediction is limited.

### Predicting LHN Odor Responses from Glomerular Connections

How important are the connections we have measured as contributors to LHN odor responses? After all, excitatory antennal lobe PNs are not the only synaptic inputs to LHNs. LHNs also receive long-range inhibition from inhibitory antennal lobe PNs, as well as local inhibition from lateral horn interneurons, and long-range excitation from other brain regions (Dolan et al., 2017; Fişek and Wilson, 2014; Liang et al., 2013; Parnas et al., 2013; Strutz et al., 2014).

To address this question, we asked whether we could predict LHN odor responses on the basis of the connections we have measured. We focused on two LHN types, V2 and V3. We knew that both receive connections from glomeruli VL2a and VA1v (Figure 4C). We therefore used odors that are reportedly selective for these glomeruli (hexanoic acid and methyl laurate; Badel et al., 2016; Dweck et al., 2015; Grosjean et al., 2011). As negative controls, we considered two glomeruli that we

Using 2-photon calcium imaging in PNs, we first verified that each odor activated its target glomerulus (Figure 8B). Methyl acetate and ethyl hexanoate were fairly selective. Methyl laurate and hexanoic acid were less selective but still were the most selective stimuli we could find for their intended targets.

To predict LHN odor responses, we projected the vector of PN odor responses onto the connectivity vector for each of these cell types. We then tested our predictions (Figure 8C) using *in vivo* whole-cell patch-clamp recordings from these LHNs (Figures 8D and 8E). This confirmed all the predicted excitatory responses. Importantly, it also confirmed all the predicted non-responses. However, we found little response to methyl laurate in V2 cells, and this differs from our prediction of an inhibitory response. We did observe weak, delayed inhibition (Figure S7), suggesting these LHNs receive odor-evoked excitation that is masking the inhibition we predicted.

To summarize, we found that excitatory PN→LHN connections can approximately predict most of the odor responses we sampled. This result implies that excitatory PN→LHN connections are a major driver of LHN odor responses. Other connections may play important roles as well, and these connections may account for some features of LHN odor responses that we did not successfully predict.

In particular, two of the LHN types in our study (ML8 and ML9) can be tentatively identified as LHN types that receive a direct connection from mushroom body output neurons (ML8 = PD2b1, ML9 = PD2a1); these LHNs have responses that are not fully predicted by PN→LHN connections alone (Dolan et al., 2017). Interestingly, Dolan et al. identified glomerulus DM1 as the strongest direct glomerular input to these LHN types,

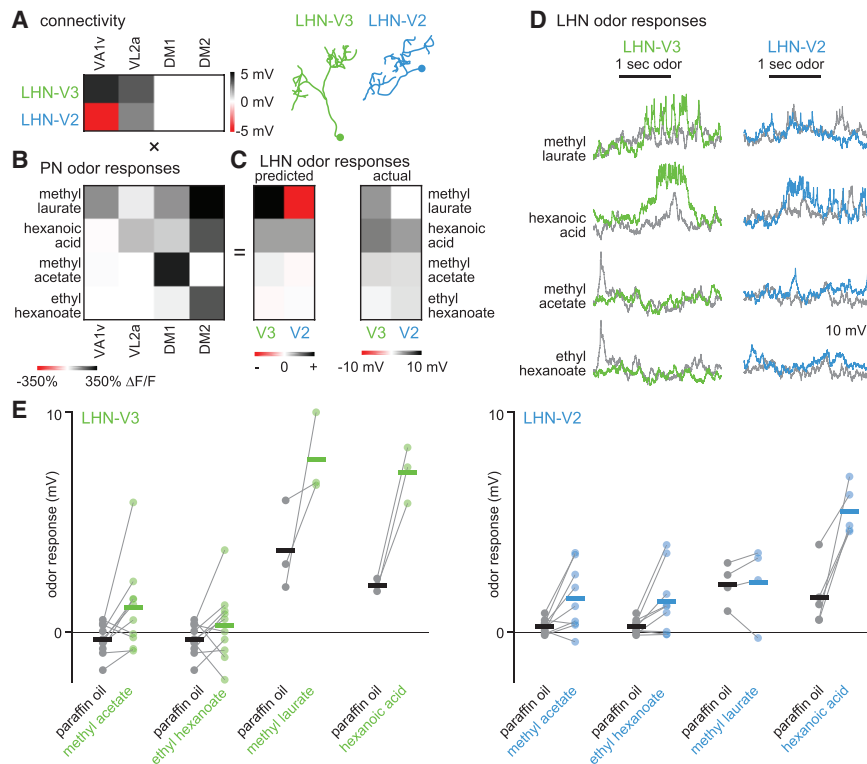


**Figure 8. Predicting LHN Odor Responses from Glomerular Connections**

(A) Connection weights from selected glomeruli onto V2 cells and V3 cells (from Figure 4C). (B) PN responses to odors were selected to stimulate these glomeruli as specifically as possible. We measured PN responses as the change in GCaMP6f fluorescence ( $\Delta F/F$ ) over the odor stimulus period. Methyl acetate and ethyl hexanoate elicited essentially no off-target responses in any glomeruli. Methyl laurate and hexanoic acid elicited responses in a few glomeruli not shown here, but these were not typically connected to V2 or V3 cells. (C) Predicted and actual LHN odor responses. Predictions (in arbitrary units) are given by the product of the matrices in (A) and (B). Actual responses are measured as the odor-evoked change in LHN voltage over the odor stimulus period, averaged across cells. (D) Examples of LHN odor responses. Responses to the odor solvent control (paraffin oil) are in gray. (E) All responses to odors and the solvent control (paraffin oil). Connected points were measured in the same experiment. We recorded from 10 V3 cells and 9 V2 cells, each in a different brain. Control data are the same for methyl acetate and ethyl hexanoate. In the case of methyl laurate and hexanoic acid, paraffin oil responses were larger because flow rates were higher, and we used matched flow rates for paraffin oil controls. See also Figure S7.

based on serial-section electron microscopy reconstructions, and this agrees with our functional measurement. Future work will be needed to understand how LHNs integrate direct PN  $\rightarrow$  LHN connections with the other inputs they receive.

## DISCUSSION

Our data reveal several hierarchical layers of circuit logic. Each governs circuit organization on a particular spatial scale—namely (1) the contributions of individual PNs, (2) the contributions of individual glomeruli, (3) the specification of individual LHN types, (4) similarities across LHN types, and (5) associations between specific glomeruli. Below we consider the significance of each layer of organization.

### The Contributions of Individual PNs

First, we found that sister PNs converge onto the same LHNs. This had been conjectured on the basis of anatomical data (Kazama and Wilson, 2009; Marin et al., 2002; Wong et al., 2002) and already demonstrated directly for one glomerulus-LHN pair (Jeanne and Wilson, 2015). Such convergence is only rarely observed in the mushroom body (Caron et al., 2013; Gruntman and Turner, 2013). Thus, in the mushroom body, individual PNs form the functional units of input, whereas in the lateral horn, entire glomeruli form the functional units of input.

Interestingly, we found that sister PNs did not (collectively) form LHN connections that were any stronger than the connections formed by single (sisterless) PNs. A recent study suggests an anatomical basis for this finding: PNs-without-sisters form

many synapses per PN-LHN connection, whereas PNs-with-sisters form fewer synapses per PN-LHN connection (Dolan et al., 2017). Our results suggest that PNs-without-sisters and PNs-with-sisters form LHN connections composed of equal total synapse numbers per glomerulus.

What is the value of sister PNs, if not to increase the total weight of a glomerulus  $\rightarrow$  LHN connection? Sister PNs are likely valuable because they improve the signal-to-noise ratio of the glomerulus-LHN connection. Sister PNs carry semi-independent noise, and their fine-scale spike timing correlations increase in the presence of an odor stimulus, which should improve LHN odor detection performance (Jeanne and Wilson, 2015).

### The Contributions of Individual Glomeruli

Second, we found that some glomeruli are over-represented at the level of LHN responses. The top glomeruli in our dataset are VA1d, VA1v, DC3, and VA6. All are narrowly tuned to olfactory stimuli (Dweck et al., 2015; Lin et al., 2016; Ronderos et al., 2014; van der Goes van Naters and Carlson, 2007).

Interestingly, in the mushroom body, inputs from certain glomeruli are also over-represented. Here, DA1 and DC3 are the dominant inputs (Caron et al., 2013), and again these glomeruli are narrowly tuned (Kurtovic et al., 2007; Ronderos et al., 2014; van der Goes van Naters and Carlson, 2007). It should be noted that Caron et al. (2013) measured connections onto only 200 Kenyon cells, and there are  $\sim$ 2000 Kenyon cells in total (Aso et al., 2009); similarly, we have measured connections onto only 110 LHNs, and there are  $\sim$ 1000 LHNs in total (M.F. and R.I.W., unpublished data). Although both studies

report partial samples, they together suggest that narrowly tuned glomeruli are over-represented in higher brain regions.

### The Specification of Individual LHN Types

Third, we found that the inputs to same-type LHNs were more correlated than the inputs to different-type LHNs. However, there was also considerable variability among same-type LHNs. The mean connectivity correlation between same-type LHNs was only about 0.6.

This finding raises the interesting question of what the genome actually specifies about a “cell type.” It might be unnecessary to precisely specify 50 glomerular connection weights onto each of 250 LHN cell types. Rather, there might be many possible combinations of adequately good connection weights, and it might be more efficient (and robust) to endow networks with compensatory mechanisms that adjust connection weights until adequate overall network performance is achieved (Marder et al., 2015).

### Similarities among LHN Types

Fourth, we found that the inputs to different-type LHNs were more correlated than we would expect by chance. In other words, there was some redundancy in the glomerular combinations that converged onto different-type LHNs. This violates the classic idea that wiring diagrams should be structured to reduce redundancy among cell types (Barlow, 1961; Simoncelli and Olshausen, 2001). The “redundancy-reduction hypothesis” predicts that different LHN types should represent completely independent combinations of glomeruli.

We found that this is not true: different LHN types can receive input from similar combinations of glomeruli. In other words, certain glomerular combinations converge onto multiple LHN types. Thus, the redundancy-reduction hypothesis does not explain this wiring diagram. Rather, there may be some benefit to over-representing certain glomerular combinations. Over-representing certain combinations should increase the informational bandwidth devoted to particular odors or blends, at the expense of other stimuli.

### Associations between Specific Glomeruli

Fifth, we identified many pairs of glomeruli that converge onto LHNs at a statistically significant rate – i.e., above what we would predict from a scheme where all glomeruli wire up independently. In some of these pairs, both glomeruli are selective for the same ligand (e.g., DA1–DL3) or highly overlapping sets of ligands (e.g., DM1–DM4). In these cases, convergence might represent a strategy to improve the signal-to-noise ratio of LHN responses by pooling signals from glomeruli that are co-activated by the same ligand.

In other cases, paired glomeruli prefer ligands that are chemically dissimilar, yet the co-occurrence of these ligands indicates a salient “odor scene.” For example, VA3 and DM2 have dissimilar odor tuning overall; what they have in common is their status as the best receptors for specific dissimilar yeast odors (2-phenyl ethanol and ethyl hexanoate). Another example is given by VA6 and DC3, two glomeruli that have almost no preferred ligands in common; what they have in common is that their best ligands (geranyl acetate and farnesol) are synthesized as part of the same biochemical pathway (Berg et al.,

2002). Yet another example is VL2a and VA1d, whose preferred ligands (phenylacetic acid and methyl palmitate) have distinct biochemical origins; what these ligands have in common is that they both promote social behaviors. In all these cases, co-activation of the glomerular pair would be highly salient, because it signals an ecologically or behaviorally relevant odor scene.

How LHNs integrate their glomerular inputs is an interesting question. There is evidence that these inputs can combine supralinearly (Fişek and Wilson, 2014; Jeanne and Wilson, 2015). Thus, we might predict that some chemical mixtures should produce especially strong responses in specific LHN types—stronger than the sum of the responses evoked by their constituents—and thus especially strong behavioral responses.

### Olfactory Scenes and Visual Scenes

In general, interesting neural computations can emerge when cells with distinct tuning converge on common postsynaptic targets. The mammalian visual system provides well-known illustrations of this idea. For example, thalamic neurons with co-linear spatial receptive fields converge to generate orientation-tuned simple cells in primary visual cortex (Reid and Alonso, 1995). Similarly, long-range corticocortical inputs with co-linear spatial receptive fields converge to endow cortical neurons with sensitivity to elongated edges (Angelucci and Bressloff, 2006; Gilbert and Li, 2013; Iacaruso et al., 2017). In these examples, convergent presynaptic inputs share one functional property (co-linearity of their receptive field centers), but they also differ from each other (in preferring nonidentical retinotopic locations). As a result, these convergent wiring patterns allow the postsynaptic cell to acquire some specificity for a higher-level visual scene feature (orientation). At the same time, this convergence confers some generality about a lower-level feature (retinotopy).

Our data suggest that the lateral horn performs analogous computations. For example, when two yeast-odor-sensing glomeruli converge, they should allow the postsynaptic cell to acquire some specificity for a higher-level odor scene feature (yeastiness). At the same time, this convergence confers some generality about a lower-level feature (chemical structure).

It is important to remember that some glomeruli participate in multiple combinations. For example, VA1d forms a significant pairwise association with five other glomeruli. This “multi-tasking” creates a larger diversity of convergence patterns than would exist if each glomerulus participated in only one combination. Of course, maximum diversity would arise if all the elemental connectivity motifs of a given size (e.g., all glomerular pairs) occurred at an equal frequency. The wiring of the lateral horn is a balance between these two extremes. This again is reminiscent of the situation in mammalian primary visual cortex. Here, the rule that convergent thalamic neurons should have co-linear receptive fields is a constraint that restricts the diversity of wiring patterns, but this rule nonetheless allows each thalamic neuron to participate in multiple wiring patterns, each potentially conferring selectivity for a different orientation.

### Solving the Problem of Dimensionality in Olfaction

In essence, the wiring of the lateral horn can be viewed as an internal model of the olfactory world. It represents a prediction of what

glomerular activity patterns will be meaningful. To see the value of this prediction, recall that the high dimensionality of glomerular space exposes the brain to the “curse of dimensionality.” There are >200,000 possible combinations of 4 glomeruli out of 50, but there are only enough neurons to sample a small fraction of these combinations. We show that the lateral horn solves this problem in a distinctive way: it over-represents those glomerular combinations that are ecologically or behaviorally relevant.

By contrast, the glomerular combinations sampled by mushroom body Kenyon cells do not embody an internal model. These patterns have no predictable meaning, because they are nearly random (Caron et al., 2013; Eichler et al., 2017), but they can acquire meaning through experience (Parnas et al., 2013). Experience-dependent plasticity occurs at the next synaptic relay, at the level of Kenyon cell output synapses, where olfactory signals are associated with contextual signals (Cohn et al., 2015; Hige et al., 2015b). In this way, the brain constructs a second internal model of the olfactory world—distinct from that of the lateral horn, because it is built on a randomly seeded basis, and it emerges differently in different brains based on different experiences (Hige et al., 2015a).

These parallel internal models—in the lateral horn and mushroom body—represent distinct strategies for coping with the curse of dimensionality in olfaction. Indeed, dimensionality is a general problem in neural systems. It is a problem for any behavioral decision that depends on many independent features of an object (e.g., visual object recognition). Our results, together with recent work on the mushroom body, show how the brain uses parallel internal models to transform signals from high-dimensional sensory space into a lower-dimensional space of complex but behaviorally relevant features. In the future, it will be interesting to discover how these parallel models are ultimately merged to generate coherent behaviors.

## STAR★METHODS

Detailed methods are provided in the online version of this paper and include the following:

- **KEY RESOURCES TABLE**
- **CONTACT FOR REAGENTS AND RESOURCE SHARING**
- **EXPERIMENTAL MODEL AND SUBJECT DETAILS**
- **METHOD DETAILS**
  - Electrophysiology
  - Multiphoton ReaChR excitation
  - Odor delivery
  - Calcium imaging of odor-evoked activity in PN
  - *In situ* neuropil staining
- **IMMUNOHISTOCHEMISTRY AND ANATOMY**
- **QUANTIFICATION AND STATISTICAL ANALYSIS**
  - Assessing errors in PN recordings and identifying glomeruli connected to LHNs
  - Quantifying glomerulus-LHN connection weights
  - Analyzing correlations between LHNs or glomeruli
  - Identifying significantly convergent pairs of glomeruli
  - Predicting connectivity from anatomy
- **DATA AND SOFTWARE AVAILABILITY**

## SUPPLEMENTAL INFORMATION

Supplemental Information includes seven figures, three tables, and one data file and can be found with this article online at <https://doi.org/10.1016/j.neuron.2018.05.011>.

## ACKNOWLEDGMENTS

We thank Greg Jefferis and Shahar Frechter for help with registering brains and for sharing information about LHN morphology, Wei-Chung Allen Lee for advice about computing axon-dendrite appositions, and Alex Wiltschko for advice on data analysis. Members of the Wilson Lab provided feedback on the manuscript. This work was supported by NIH grants R01 DC008174 to R.I.W. and F32 NS083262 to J.M.J. M.F. was an HHMI International Student Research Fellow. R.I.W. is an HHMI Investigator. Confocal microscopy was funded in part by NIH grant P30 NS072030.

## AUTHOR CONTRIBUTIONS

J.M.J., M.F., and R.I.W. designed the study. M.F. performed much of the methodology development and collected most of the data in Figures 1 and S5, as well as some data in Figure 3. J.M.J. optimized some methodologies and performed all the other experiments in the study. J.M.J. designed and performed the data analysis. J.M.J. and M.F. hand-traced all the LHN morphologies. J.M.J., M.F., and R.I.W. wrote the manuscript.

## DECLARATION OF INTERESTS

The authors declare no competing interests.

Received: March 3, 2018

Revised: April 19, 2018

Accepted: May 4, 2018

Published: June 14, 2018

## REFERENCES

- Angelucci, A., and Bressloff, P.C. (2006). Contribution of feedforward, lateral and feedback connections to the classical receptive field center and extra-classical receptive field surround of primate V1 neurons. *Prog. Brain Res.* 154, 93–120.
- Antonelli, A., Castellari, L., Zambonelli, C., and Carnacini, A. (1999). Yeast influence on volatile composition of wines. *J. Agric. Food Chem.* 47, 1139–1144.
- Apicella, A., Yuan, Q., Scanziani, M., and Isaacson, J.S. (2010). Pyramidal cells in piriform cortex receive convergent input from distinct olfactory bulb glomeruli. *J. Neurosci.* 30, 14255–14260.
- Aso, Y., Grübel, K., Busch, S., Friedrich, A.B., Siwanowicz, I., and Tanimoto, H. (2009). The mushroom body of adult *Drosophila* characterized by GAL4 drivers. *J. Neurogenet.* 23, 156–172.
- Badel, L., Ohta, K., Tsuchimoto, Y., and Kazama, H. (2016). Decoding of context-dependent olfactory behavior in *Drosophila*. *Neuron* 91, 155–167.
- Barlow, H. (1961). Possible principles underlying the transformation of sensory messages. In *Sensory Communication*, W.A. Rosenblith, ed. (MIT Press), pp. 217–234.
- Becher, P.G., Flick, G., Rozpędowska, E., Schmidt, A., Hagman, A., Lebreton, S., Larsson, M.C., Hansson, B.S., Piskur, J., Witzgall, P., and Bengtsson, B. (2012). Yeast, not fruit volatiles mediate *Drosophila melanogaster* attraction, oviposition and development. *Funct. Ecol.* 26, 822–828.
- Bell, J.S., and Wilson, R.I. (2016). Behavior reveals selective summation and max pooling among olfactory processing channels. *Neuron* 91, 425–438.
- Berg, J.M., Tymoczko, J.L., and Stryer, L. (2002). *Biochemistry*, 5th Edition. (W.H. Freeman).
- Bhandawat, V., Olsen, S.R., Gouwens, N.W., Schlieff, M.L., and Wilson, R.I. (2007). Sensory processing in the *Drosophila* antennal lobe increases reliability

- and separability of ensemble odor representations. *Nat. Neurosci.* **10**, 1474–1482.
- Caron, S.J., Ruta, V., Abbott, L.F., and Axel, R. (2013). Random convergence of olfactory inputs in the *Drosophila* mushroom body. *Nature* **497**, 113–117.
- Carrau, F.M., Medina, K., Boido, E., Farina, L., Gaggero, C., Dellacassa, E., Versini, G., and Henschke, P.A. (2005). De novo synthesis of monoterpenes by *Saccharomyces cerevisiae* wine yeasts. *FEMS Microbiol. Lett.* **243**, 107–115.
- Carson, C.F., Mee, B.J., and Riley, T.V. (2002). Mechanism of action of *Melaleuca alternifolia* (tea tree) oil on *Staphylococcus aureus* determined by time-kill, lysis, leakage, and salt tolerance assays and electron microscopy. *Antimicrob. Agents Chemother.* **46**, 1914–1920.
- Chiang, A.S., Lin, C.Y., Chuang, C.C., Chang, H.M., Hsieh, C.H., Yeh, C.W., Shih, C.T., Wu, J.J., Wang, G.T., Chen, Y.C., et al. (2011). Three-dimensional reconstruction of brain-wide wiring networks in *Drosophila* at single-cell resolution. *Curr. Biol.* **21**, 1–11.
- Christiaens, J.F., Franco, L.M., Cools, T.L., De Meester, L., Michiels, J., Wenseleers, T., Hassan, B.A., Yaksi, E., and Verstrepen, K.J. (2014). The fungal aroma gene ATF1 promotes dispersal of yeast cells through insect vectors. *Cell Rep.* **9**, 425–432.
- Cleland, T.A. (2014). Construction of odor representations by olfactory bulb microcircuits. *Prog. Brain Res.* **208**, 177–203.
- Cohn, R., Morante, I., and Ruta, V. (2015). Coordinated and compartmentalized neuromodulation shapes sensory processing in *Drosophila*. *Cell* **163**, 1742–1755.
- Costa, M., Manton, J.D., Ostrovsky, A.D., Prohaska, S., and Jefferis, G.S. (2016). NBLAST: Rapid, sensitive comparison of neuronal structure and construction of neuron family databases. *Neuron* **91**, 293–311.
- Couto, A., Alenius, M., and Dickson, B.J. (2005). Molecular, anatomical, and functional organization of the *Drosophila* olfactory system. *Curr. Biol.* **15**, 1535–1547.
- Davison, I.G., and Ehlers, M.D. (2011). Neural circuit mechanisms for pattern detection and feature combination in olfactory cortex. *Neuron* **70**, 82–94.
- de Bruyne, M., Clyne, P.J., and Carlson, J.R. (1999). Odor coding in a model olfactory organ: The *Drosophila* maxillary palp. *J. Neurosci.* **19**, 4520–4532.
- de Bruyne, M., Foster, K., and Carlson, J.R. (2001). Odor coding in the *Drosophila* antenna. *Neuron* **30**, 537–552.
- Dolan, M.J., Belliard-Guérin, G., Aso, Y., Bates, A.S., Frechter, S., Wong, A., Hammad, A., Rubin, G.M., Préat, T., Plaçais, P.-Y., and Jefferis, G.S.X.E. (2017). Memory retrieval recruits both innate and learned olfactory processing centres in *Drosophila*. *bioRxiv*. <https://doi.org/10.1101/167312>.
- Dugelay, I., Gunata, Z., Sapis, J.C., Baumes, R., and Bayonove, C. (1992). Etude de l'origine du citronellol dans les vins. *J. Int. Sci. Vigne Vin* **26**, 177–184.
- Dweck, H.K., Ebrahim, S.A., Kromann, S., Bown, D., Hillbur, Y., Sachse, S., Hansson, B.S., and Stensmyr, M.C. (2013). Olfactory preference for egg laying on citrus substrates in *Drosophila*. *Curr. Biol.* **23**, 2472–2480.
- Dweck, H.K., Ebrahim, S.A., Thoma, M., Mohamed, A.A., Keese, I.W., Trona, F., Lavista-Llanos, S., Svatoš, A., Sachse, S., Knaden, M., and Hansson, B.S. (2015). Pheromones mediating copulation and attraction in *Drosophila*. *Proc. Natl. Acad. Sci. USA* **112**, E2829–E2835.
- Ebrahim, S.A., Dweck, H.K., Stöckl, J., Hofferberth, J.E., Trona, F., Weniger, K., Rybak, J., Seki, Y., Stensmyr, M.C., Sachse, S., et al. (2015). *Drosophila* avoids parasitoids by sensing their semiochemicals via a dedicated olfactory circuit. *PLoS Biol.* **13**, e1002318.
- Eichler, K., Li, F., Litwin-Kumar, A., Park, Y., Andrade, I., Schneider-Mizell, C.M., Saumweber, T., Huser, A., Eschbach, C., Gerber, B., et al. (2017). The complete connectome of a learning and memory centre in an insect brain. *Nature* **548**, 175–182.
- Ejima, A., Smith, B.P., Lucas, C., van der Goes van Naters, W., Miller, C.J., Carlson, J.R., Levine, J.D., and Griffith, L.C. (2007). Generalization of courtship learning in *Drosophila* is mediated by cis-vaccenyl acetate. *Curr. Biol.* **17**, 599–605.
- El Hadi, M.A.M., Zhang, F.-J., Wu, F.-F., Zhou, C.-H., and Tao, J. (2013). Advances in fruit aroma volatile research. *Molecules* **18**, 8200–8229.
- Fairhall, A. (2014). The receptive field is dead. Long live the receptive field? *Curr. Opin. Neurobiol.* **25**, ix–xii.
- Fişek, M., and Wilson, R.I. (2014). Stereotyped connectivity and computations in higher-order olfactory neurons. *Nat. Neurosci.* **17**, 280–288.
- Frechter, S., Bates, A.S., Tootoonian, S., Dolan, M.-J., Manton, J.D., Jamasb, A., Kohl, J., Bock, D., and Jefferis, G.S.X.E. (2018). Functional and anatomical specificity in a higher olfactory centre. *bioRxiv*. <https://doi.org/10.1101/336982>.
- Gerhard, S., Andrade, I., Fetter, R.D., Cardona, A., and Schneider-Mizell, C.M. (2017). Conserved neural circuit structure across *Drosophila* larval development revealed by comparative connectomics. *eLife* **6**, e29089.
- Ghosh, S., Larson, S.D., Hefzi, H., Marnoy, Z., Cutforth, T., Dokka, K., and Baldwin, K.K. (2011). Sensory maps in the olfactory cortex defined by long-range viral tracing of single neurons. *Nature* **472**, 217–220.
- Gilbert, C.D., and Li, W. (2013). Top-down influences on visual processing. *Nat. Rev. Neurosci.* **14**, 350–363.
- Goldman, A.L., Van der Goes van Naters, W., Lessing, D., Warr, C.G., and Carlson, J.R. (2005). Coexpression of two functional odor receptors in one neuron. *Neuron* **45**, 661–666.
- Goodman, M.B., and Lockery, S.R. (2000). Pressure polishing: A method for re-shaping patch pipettes during fire polishing. *J. Neurosci. Methods* **100**, 13–15.
- Grabe, V., Strutz, A., Baschwitz, A., Hansson, B.S., and Sachse, S. (2015). Digital in vivo 3D atlas of the antennal lobe of *Drosophila melanogaster*. *J. Comp. Neurol.* **523**, 530–544.
- Grabe, V., Baschwitz, A., Dweck, H.K.M., Lavista-Llanos, S., Hansson, B.S., and Sachse, S. (2016). Elucidating the neuronal architecture of olfactory glomeruli in the *Drosophila* antennal lobe. *Cell Rep.* **16**, 3401–3413.
- Grosjean, Y., Rytz, R., Farine, J.P., Abuin, L., Cortot, J., Jefferis, G.S., and Benton, R. (2011). An olfactory receptor for food-derived odours promotes male courtship in *Drosophila*. *Nature* **478**, 236–240.
- Gruntman, E., and Turner, G.C. (2013). Integration of the olfactory code across dendritic claws of single mushroom body neurons. *Nat. Neurosci.* **16**, 1821–1829.
- Ha, T.S., and Smith, D.P. (2006). A pheromone receptor mediates 11-cis-vaccenyl acetate-induced responses in *Drosophila*. *J. Neurosci.* **26**, 8727–8733.
- Haddad, R., Khan, R., Takahashi, Y.K., Mori, K., Harel, D., and Sobel, N. (2008). A metric for odorant comparison. *Nat. Methods* **5**, 425–429.
- Hallam, E.A., and Carlson, J.R. (2006). Coding of odors by a receptor repertoire. *Cell* **125**, 143–160.
- Hige, T., Aso, Y., Rubin, G.M., and Turner, G.C. (2015a). Plasticity-driven individualization of olfactory coding in mushroom body output neurons. *Nature* **526**, 258–262.
- Hige, T., Aso, Y., Modi, M.N., Rubin, G.M., and Turner, G.C. (2015b). Heterosynaptic plasticity underlies aversive olfactory learning in *Drosophila*. *Neuron* **88**, 985–998.
- Hong, E.J., and Wilson, R.I. (2015). Simultaneous encoding of odors by channels with diverse sensitivity to inhibition. *Neuron* **85**, 573–589.
- Iacaruso, M.F., Gasler, I.T., and Hofer, S.B. (2017). Synaptic organization of visual space in primary visual cortex. *Nature* **547**, 449–452.
- Inagaki, H.K., Jung, Y., Hoopfer, E.D., Wong, A.M., Mishra, N., Lin, J.Y., Tsien, R.Y., and Anderson, D.J. (2014). Optogenetic control of *Drosophila* using a red-shifted channelrhodopsin reveals experience-dependent influences on courtship. *Nat. Methods* **11**, 325–332.
- Inoue, Y., Shiraishi, A., Hada, T., Hirose, K., Hamashima, H., and Shimada, J. (2004). The antibacterial effects of terpene alcohols on *Staphylococcus aureus* and their mode of action. *FEMS Microbiol. Lett.* **237**, 325–331.
- Ito, K., Shinomiya, K., Ito, M., Armstrong, J.D., Boyan, G., Hartenstein, V., Harzsch, S., Heisenberg, M., Homberg, U., Jenett, A., et al.; Insect Brain

- Name Working Group (2014). A systematic nomenclature for the insect brain. *Neuron* 81, 755–765.
- Jeanne, J.M., and Wilson, R.I. (2015). Convergence, divergence, and reconvergence in a feedforward network improves neural speed and accuracy. *Neuron* 88, 1014–1026.
- Jefferis, G.S.X.E. (2014). JFRC2 Template Brain. <https://doi.org/10.5281/zenodo.10567>.
- Jefferis, G.S.X.E., and Manton, J.D. (2017). NeuroAnatomy Toolbox. <https://doi.org/10.5281/zenodo.10171>.
- Jefferis, G.S., Potter, C.J., Chan, A.M., Marin, E.C., Rohlfsing, T., Maurer, C.R., Jr., and Luo, L. (2007). Comprehensive maps of *Drosophila* higher olfactory centers: Spatially segregated fruit and pheromone representation. *Cell* 128, 1187–1203.
- Jenett, A., Rubin, G.M., Ngo, T.T., Shepherd, D., Murphy, C., Dionne, H., Pfeiffer, B.D., Cavallaro, A., Hall, D., Jeter, J., et al. (2012). A GAL4-driver line resource for *Drosophila* neurobiology. *Cell Rep.* 2, 991–1001.
- Kakarla, S., and Ganjewala, D. (2009). Antimicrobial activity of essential oils of four lemongrass (*Cymbopogon flexuosus* Steud) varieties. *Med. Aromat. Plant Sci. Biotechnol.* 3, 107–109.
- Kazama, H., and Wilson, R.I. (2009). Origins of correlated activity in an olfactory circuit. *Nat. Neurosci.* 12, 1136–1144.
- Kazemi, M., Mousavi, E., and Kharestani, R. (2012). Chemical compositions and antimicrobial activities of essential oils of *Varthemia persica*, *Foeniculum vulgare* and *Ferula lycia*. *Curr. Res. Bacteriol.* 5, 42–52.
- Kim, Y., Cho, J.Y., Kuk, J.H., Moon, J.H., Cho, J.I., Kim, Y.C., and Park, K.H. (2004). Identification and antimicrobial activity of phenylacetic acid produced by *Bacillus licheniformis* isolated from fermented soybean, Chungkook-Jang. *Curr. Microbiol.* 48, 312–317.
- Kohl, J., Ostrovsky, A.D., Frechter, S., and Jefferis, G.S. (2013). A bidirectional circuit switch reroutes pheromone signals in male and female brains. *Cell* 155, 1610–1623.
- Kreher, S.A., Kwon, J.Y., and Carlson, J.R. (2005). The molecular basis of odor coding in the *Drosophila* larva. *Neuron* 46, 445–456.
- Kurtovic, A., Widmer, B., and Dickson, B.J. (2007). A single class of olfactory neurons mediates behavioural responses to a *Drosophila* sex pheromone. *Nature* 446, 542–546.
- Lai, S.L., Awasaki, T., Ito, K., and Lee, T. (2008). Clonal analysis of *Drosophila* antennal lobe neurons: Diverse neuronal architectures in the lateral neuroblast lineage. *Development* 135, 2883–2893.
- Laisue, P.P., Reiter, C., Hiesinger, P.R., Halter, S., Fischbach, K.F., and Stocker, R.F. (1999). Three-dimensional reconstruction of the antennal lobe in *Drosophila melanogaster*. *J. Comp. Neurol.* 405, 543–552.
- Lebreton, S., Grabe, V., Omondi, A.B., Ignell, R., Becher, P.G., Hansson, B.S., Sachse, S., and Witzgall, P. (2014). Love makes smell blind: Mating suppresses pheromone attraction in *Drosophila* females via Or65a olfactory neurons. *Sci. Rep.* 4, 7119.
- Liang, L., Li, Y., Potter, C.J., Yizhar, O., Deisseroth, K., Tsien, R.W., and Luo, L. (2013). GABAergic projection neurons route selective olfactory inputs to specific higher-order neurons. *Neuron* 79, 917–931.
- Lin, J.Y., Knutsen, P.M., Muller, A., Kleinfeld, D., and Tsien, R.Y. (2013). ReaChR: A red-shifted variant of channelrhodopsin enables deep transcranial optogenetic excitation. *Nat. Neurosci.* 16, 1499–1508.
- Lin, H.H., Cao, D.S., Sethi, S., Zeng, Z., Chin, J.S.R., Chakraborty, T.S., Shepherd, A.K., Nguyen, C.A., Yew, J.Y., Su, C.Y., and Wang, J.W. (2016). Hormonal modulation of pheromone detection enhances male courtship success. *Neuron* 90, 1272–1285.
- Litwin-Kumar, A., Harris, K.D., Axel, R., Sompolinsky, H., and Abbott, L.F. (2017). Optimal degrees of synaptic connectivity. *Neuron* 93, 1153–1164.e7.
- Liu, W., Liang, X., Gong, J., Yang, Z., Zhang, Y.H., Zhang, J.X., and Rao, Y. (2011). Social regulation of aggression by pheromonal activation of Or65a olfactory neurons in *Drosophila*. *Nat. Neurosci.* 14, 896–902.
- Longair, M.H., Baker, D.A., and Armstrong, J.D. (2011). Simple Neurite Tracer: Open source software for reconstruction, visualization and analysis of neuronal processes. *Bioinformatics* 27, 2453–2454.
- Luo, S.X., Axel, R., and Abbott, L.F. (2010). Generating sparse and selective third-order responses in the olfactory system of the fly. *Proc. Natl. Acad. Sci. USA* 107, 10713–10718.
- Malnic, B., Hirono, J., Sato, T., and Buck, L.B. (1999). Combinatorial receptor codes for odors. *Cell* 96, 713–723.
- Marder, E., Goeritz, M.L., and Otopalik, A.G. (2015). Robust circuit rhythms in small circuits arise from variable circuit components and mechanisms. *Curr. Opin. Neurobiol.* 31, 156–163.
- Marin, E.C., Jefferis, G.S., Komiyama, T., Zhu, H., and Luo, L. (2002). Representation of the glomerular olfactory map in the *Drosophila* brain. *Cell* 109, 243–255.
- Min, S., Ai, M., Shin, S.A., and Suh, G.S. (2013). Dedicated olfactory neurons mediating attraction behavior to ammonia and amines in *Drosophila*. *Proc. Natl. Acad. Sci. USA* 110, E1321–E1329.
- Miyamichi, K., Amat, F., Moussavi, F., Wang, C., Wickersham, I., Wall, N.R., Taniguchi, H., Tasic, B., Huang, Z.J., He, Z., et al. (2011). Cortical representations of olfactory input by trans-synaptic tracing. *Nature* 472, 191–196.
- Münch, D., and Galizia, C.G. (2016). DoOR 2.0—comprehensive mapping of *Drosophila melanogaster* odorant responses. *Sci. Rep.* 6, 21841.
- Olsen, S.R., Bhandawat, V., and Wilson, R.I. (2010). Divisive normalization in olfactory population codes. *Neuron* 66, 287–299.
- Parnas, M., Lin, A.C., Huetteroth, W., and Miesenböck, G. (2013). Odor discrimination in *Drosophila*: From neural population codes to behavior. *Neuron* 79, 932–944.
- Pitts, S., Pelser, E., Meeks, J., and Smith, D. (2016). Odorant responses and courtship behaviors influenced by at4 neurons in *Drosophila*. *PLoS ONE* 11, e0162761.
- Reid, R.C., and Alonso, J.M. (1995). Specificity of monosynaptic connections from thalamus to visual cortex. *Nature* 378, 281–284.
- Ronderos, D.S., Lin, C.C., Potter, C.J., and Smith, D.P. (2014). Farnesol-detecting olfactory neurons in *Drosophila*. *J. Neurosci.* 34, 3959–3968.
- Ruta, V., Datta, S.R., Vasconcelos, M.L., Freeland, J., Looger, L.L., and Axel, R. (2010). A dimorphic pheromone circuit in *Drosophila* from sensory input to descending output. *Nature* 468, 686–690.
- Scheidler, N.H., Liu, C., Hamby, K.A., Zalom, F.G., and Syed, Z. (2015). Volatile codes: Correlation of olfactory signals and reception in *Drosophila*-yeast chemical communication. *Sci. Rep.* 5, 14059.
- Schindelin, J., Arganda-Carreras, I., Frise, E., Kaynig, V., Longair, M., Pietzsch, T., Preibisch, S., Rueden, C., Saalfeld, S., Schmid, B., et al. (2012). Fiji: An open-source platform for biological-image analysis. *Nat. Methods* 9, 676–682.
- Schlieff, M.L., and Wilson, R.I. (2007). Olfactory processing and behavior downstream from highly selective receptor neurons. *Nat. Neurosci.* 10, 623–630.
- Silbering, A.F., Rytz, R., Grosjean, Y., Abuin, L., Ramdya, P., Jefferis, G.S., and Benton, R. (2011). Complementary function and integrated wiring of the evolutionarily distinct *Drosophila* olfactory subsystems. *J. Neurosci.* 31, 13357–13375.
- Simoncelli, E.P., and Olshausen, B.A. (2001). Natural image statistics and neural representation. *Annu. Rev. Neurosci.* 24, 1193–1216.
- Soković, M., Glamočlija, J., Marin, P.D., Brkić, D., and van Griensven, L.J.L.D. (2010). Antibacterial effects of the essential oils of commonly consumed medicinal herbs using an in vitro model. *Molecules* 15, 7532–7546.
- Sosulski, D.L., Bloom, M.L., Cutforth, T., Axel, R., and Datta, S.R. (2011). Distinct representations of olfactory information in different cortical centres. *Nature* 472, 213–216.
- Stepanyants, A., and Chklovskii, D.B. (2005). Neurogeometry and potential synaptic connectivity. *Trends Neurosci.* 28, 387–394.

- Stocker, R.F., Heimbeck, G., Gendre, N., and de Belle, J.S. (1997). Neuroblast ablation in *Drosophila* P[GAL4] lines reveals origins of olfactory interneurons. *J. Neurobiol.* *32*, 443–456.
- Strutz, A., Soelter, J., Baschwitz, A., Farhan, A., Grabe, V., Rybak, J., Knaden, M., Schmucker, M., Hansson, B.S., and Sachse, S. (2014). Decoding odor quality and intensity in the *Drosophila* brain. *eLife* *3*, e04147.
- Su, C.Y., Menuz, K., and Carlson, J.R. (2009). Olfactory perception: Receptors, cells, and circuits. *Cell* *139*, 45–59.
- Surburg, H., and Panten, J. (2006). *Common Fragrance and Flavor Materials*, 5th Edition. (Wiley-VCH).
- Tanaka, N.K., Awasaki, T., Shimada, T., and Ito, K. (2004). Integration of chemosensory pathways in the *Drosophila* second-order olfactory centers. *Curr. Biol.* *14*, 449–457.
- Tobin, W.F., Wilson, R.I., and Lee, W.A. (2017). Wiring variations that enable and constrain neural computation in a sensory microcircuit. *eLife* *6*, e24838.
- Tsakiris, A., Koutinas, A.A., Psarianos, C., Kourkoutas, Y., and Bekatorou, A. (2010). A new process for wine production by penetration of yeast in uncrushed frozen grapes. *Appl. Biochem. Biotechnol.* *162*, 1109–1121.
- van der Goes van Naters, W., and Carlson, J.R. (2007). Receptors and neurons for fly odors in *Drosophila*. *Curr. Biol.* *17*, 606–612.
- Wang, L., and Anderson, D.J. (2010). Identification of an aggression-promoting pheromone and its receptor neurons in *Drosophila*. *Nature* *463*, 227–231.
- Wong, A.M., Wang, J.W., and Axel, R. (2002). Spatial representation of the glomerular map in the *Drosophila* protocerebrum. *Cell* *109*, 229–241.
- Yu, H.H., Kao, C.F., He, Y., Ding, P., Kao, J.C., and Lee, T. (2010). A complete developmental sequence of a *Drosophila* neuronal lineage as revealed by twin-spot MARCM. *PLoS Biol.* *8*. Published online August 24, 2010. <https://doi.org/10.1371/journal.pbio.1000461>.
- Zhang, B., and Chen, K.-S. (2014). Aroma Volatiles. In *Fruit Ripening: Physiology, Signalling, and Genomics*, P. Nath, M. Bouzayen, A.K. Mattoo, and J.C. Pech, eds. (CAB International), pp. 63–80.
- Zheng, Z., Lauritzen, J.S., Eric Perlman, E., Robinson, C.G., Nichols, M., Milkie, D., Torrens, O., Price, J., Fisher, C.B., Sharifi, N., et al. (2017). A complete electron microscopy volume of the brain of adult *Drosophila melanogaster*. *bioRxiv*. <https://doi.org/10.1101/140905>.

## STAR★METHODS

### KEY RESOURCES TABLE

REAGENT or RESOURCE	SOURCE	IDENTIFIER
<b>Antibodies</b>		
mouse anti-Bruchpilot antibody	Developmental Studies Hybridoma Bank	Cat#nc82 s
goat anti-mouse secondary antibody, Alexa Fluor 633 conjugate	Invitrogen	Cat#A21050
<b>Chemicals, Peptides, and Recombinant Proteins</b>		
streptavidin, Alexa Fluor 568 conjugate	Invitrogen	Cat#S11226
$\alpha$ -bungarotoxin, Alexa Fluor 488 conjugate	Invitrogen	Cat#B13422
Alexa Fluor 568 hydrazide	Invitrogen	Cat# A10437
<b>Deposited Data</b>		
Traced and registered antennal lobe projection neuron axons	Grosjean et al., 2011	<a href="http://flybrain.mrc-lmb.cam.ac.uk/si/grosjean11/MyNeuronsFCIR.rda">http://flybrain.mrc-lmb.cam.ac.uk/si/grosjean11/MyNeuronsFCIR.rda</a>
<b>Experimental Models: Organisms/Strains</b>		
GH146-Gal4	Bloomington Drosophila Stock Center (BDSC)	RRID:BDSC_30026
Mz671-Gal4	G. Technau (Johannes Gutenberg University Mainz)	Flybase FBti0058539
NP6099-Gal4	Kyoto Center for Drosophila Genomics and Genetic Resources	RRID:DGGR_105125
R12H12-Gal4(attP2)	BDSC	RRID:BDSC_48534
R22A12-Gal4(attP2)	BDSC	RRID:BDSC_49298
R25A01-Gal4(attP2)	BDSC	RRID:BDSC_49102
R28A10-Gal4(attP2)	BDSC	RRID:BDSC_48074
R29E11-Gal4(attP2)	BDSC	RRID:BDSC_49489
R39D07-Gal4(attP2)	BDSC	RRID:BDSC_50046
R44G08-Gal4(attP2)	BDSC	RRID:BDSC_50216
R54G12-Gal4(attP2)	BDSC	RRID:BDSC_41280
R55C09-Gal4(attP2)	BDSC	RRID:BDSC_39107
R67B03-Gal4(attP2)	BDSC	RRID:BDSC_39403
R73B12-Gal4(attP2)	BDSC	RRID:BDSC_39814
R76E07-Gal4(attP2)	BDSC	RRID:BDSC_39929
R82F03-Gal4(attP2)	BDSC	RRID:BDSC_40156
R94B04-Gal4(attP2)	BDSC	RRID:BDSC_40675
UAS-ReaChR:mCitrine(VK00005)	BDSC	RRID:BDSC_53749
UAS-ReaChR:mCitrine(su(Hw)attP5)	BDSC	RRID:BDSC_53748
UAS-GCaMP6f(VK00005)	BDSC	RRID:BDSC_52869
20XUAS-IVS-mCD8::GFP(attP2)	BDSC	RRID:BDSC_32194
<b>Software and Algorithms</b>		
ScanImage 3.7	Vidrio Technologies	
Simple Neurite Tracer plugin (Fiji)	Longair et al., 2011	<a href="https://imagej.net/Simple_Neurite_Tracer">https://imagej.net/Simple_Neurite_Tracer</a>
Computational Morphometry Toolkit	Neuroimaging Informatics Tools and Resources Clearinghouse	<a href="https://www.nitrc.org/projects/cmtk/">https://www.nitrc.org/projects/cmtk/</a>
NBLAST	Costa et al., 2016	<a href="https://github.com/jefferislab/nat.nblast">https://github.com/jefferislab/nat.nblast</a>
NeuroAnatomy Toolbox	Jefferis and Manton, 2017	<a href="https://github.com/jefferis/nat">https://github.com/jefferis/nat</a>

## CONTACT FOR REAGENTS AND RESOURCE SHARING

Further information and requests for resources and reagents should be directed to and will be fulfilled by the Lead Contact Rachel Wilson ([rachel\\_wilson@hms.harvard.edu](mailto:rachel_wilson@hms.harvard.edu)).

## EXPERIMENTAL MODEL AND SUBJECT DETAILS

Flies (*Drosophila melanogaster*) were raised on conventional cornmeal agar medium supplemented with rehydrated potato flakes (Carolina Biological Supply) and yeast under a 12 h light, 12 h dark cycle at 25°C. All glomerular photostimulation experiments were performed on adult female flies 2-3 days after eclosion. The exceptions were two recordings performed in male brains. Results for females and males were similar and so were combined. We used 2-3 day old flies because we found that younger flies had inconsistent ReaChR expression across flies. Four to six hours after eclosion, flies were transferred to small vials containing rehydrated potato flakes mixed with 200  $\mu$ L of all-trans-retinal stock solution (Sigma; 35 mM in ethanol). All odor-tuning experiments were performed on adult female flies 1-2 days after eclosion.

The genotypes used for LHN odor-tuning experiments (Figures 3 and 8C–8E) were:

R39D07-Gal4/UAS-20x-GFP  
R67B03-Gal4/UAS-20x-GFP

Additional data in Figure 3 were taken from a published study (Fişek and Wilson, 2014); these experiments used the following two genotypes:

NP6099-Gal4,UAS-CD8:GFP  
Mz671-Gal4,UAS-CD8:GFP

The genotypes used for PN recordings in stimulation validation experiments (Figure 1) were:

GH146-Gal4/+ ; UAS-ReaChR:mCitrine(VK00005)/+  
GH146-Gal4/+ ; LHN-Gal4/UAS-ReaChR:mCitrine(VK00005)  
UAS-ReaChR:mCitrine(su(Hw)attP5)/GH146-Gal4 ; LHN-Gal4

where *LHN-Gal4* refers to the specific Gal4 lines listed in Figure 4C. Results for these genotypes were similar and so were combined in our PN analyses. We found that *GH146-Gal4* drives expression in PNs in 39 out of 50 olfactory glomeruli in the antennal lobe. These are the 37 olfactory glomeruli listed in Grabe et al. (2015), plus DA3, which is listed as *GH146*-negative by Grabe et al., and VL1, which is described by Grabe et al. as containing no *GH146*-positive cholinergic PNs, but which does contain at least one *GH146*-positive GABAergic PN (Lai et al., 2008; Marin et al., 2002; Wong et al., 2002).

The genotypes used for LHN recordings in connectivity-mapping experiments (Figures 2, 4, 5, 6, and 7) were:

GH146-Gal4/+ ; LHN-Gal4/UAS-ReaChR:mCitrine(VK00005)  
UAS-ReaChR:mCitrine(su(Hw)attP5)/GH146-Gal4 ; LHN-Gal4

The genotype used for PN calcium imaging experiments (Figure 8B) was:

GH146-Gal4/+ ; UAS-GCaMP6f/+

One Gal4 line used to drive expression in LHNs (*NP6099*) has been described previously (Fişek and Wilson, 2014; Tanaka et al., 2004) and was obtained from the Kyoto Center for *Drosophila* Genomics and Genetic Resources (stock #105125). The rest of the Gal4 lines used to drive expression in LHNs were identified by us as part of this study, based on our visual screens of the Janelia Research Campus FlyLight images (Jenett et al., 2012) and were obtained from the Bloomington *Drosophila* Stock Center; these Gal4 lines are *82F03* (Bloomington #40156), *22A12* (#49298), *25A01* (#49102), *28A10* (#48074), *12H12* (#48534), *94B04* (#40675), *67B03* (#39403), *76E07* (#39929), *54G12* (#41280), *39D07* (#50046), *29E11* (#49489), *73B12* (#39814), *55C09* (#39107), and *44G08* (#50216). Several of the LHNs we recorded from turned out to express Gal4 under the control of *GH146-Gal4* itself, and these LHNs are listed in Figure 4C as “GH146.”

*UAS-ReaChR:mCitrine(su(Hw)attP5)* and *UAS-ReaChR:mCitrine(VK00005)* were obtained from the BDRC (#53748 and #53749).

## METHOD DETAILS

### Electrophysiology

For the *in vivo* odor-tuning experiments, flies were prepared and dissected as previously described (Fişek and Wilson, 2014). For the glomerular photostimulation experiments, each fly was cold-anesthetized and the brain was dissected out of the head capsule using fine forceps and electrolytically sharpened tungsten wires. The brain was then pinned to a Sylgard-coated dish using two sharpened

tungsten wires. A small triangular wedge of Sylgard was then placed under each brain to provide additional support. This wedge also allowed the precise adjustment of the brain's orientation, allowing us to target LHNs with different somata locations. The brain was positioned anterior-side up to target anterior somata and dorsal-side up to target posterior somata. The dorsal-side up orientation was necessary to maintain good optical access to the antennal lobe while recording posterior LHNs. Control recordings from PNs (Figure 1) were recorded from brains in both orientations; there was no effect of brain orientation on PN responses to glomerular photostimulation.

Whole-cell patch clamp recordings were performed as previously described (Jeanne and Wilson, 2015). One neuron was recorded per brain. The internal patch pipette solution contained (in mM): 140 potassium aspartate, 10 4-(2-hydroxyethyl)-1-piperazineethanesulfonic acid, 4 MgATP, 0.5 Na<sub>3</sub>GTP, 1 ethylene glycol tetraacetic acid, 1 KCl, 13 biocytin hydrazide, and 50 Alexa Fluor 568 (pH adjusted to 7.3, osmolarity adjusted to ~268 mOsm). The external saline contained (in mM): 103 NaCl, 3 KCl, 5 N-tris(hydroxymethyl) methyl-2-aminoethane-sulfonic acid, 8 trehalose, 10 glucose, 26 NaHCO<sub>3</sub>, 1 NaH<sub>2</sub>PO<sub>4</sub>, 1.5 CaCl<sub>2</sub> and 4 MgCl<sub>2</sub> (osmolarity adjusted to 270–273 mOsm). The saline was bubbled with 95% O<sub>2</sub> and 5% CO<sub>2</sub> and reached an equilibrium pH of 7.3. Saline was superfused continuously over the brain during the recording. Recordings were obtained with an Axopatch 200B model amplifier with a CV-203BU head stage and were acquired with custom-written MATLAB routines. Recorded voltages were low-pass filtered at 5 kHz before digitization at 10 kHz. Patch pipettes were made from borosilicate glass (Sutter; 1.5-mm outer diameter, 0.86-mm inner diameter) and were pressure-polished to create a cone-shaped taper with relatively low overall resistance, given the diameter of the tip (Goodman and Lockery, 2000). The estimated final pipette tip opening was < 1 μm in diameter, and the pipette resistance was between 6 and 15 MΩ.

### Multiphoton ReaChR excitation

After a whole-cell current-clamp recording was established, an image stack of ReaChR:mCitrine expression in the antennal lobe was obtained. The image stack consisted of 80 optical sections with 1-μm spacing, and was acquired at 940 nm using a custom-built two-photon laser scanning microscope incorporating a Mai Tai HP Ti:Sapphire laser (Spectra-Physics). The microscope was equipped with a 20 × water-immersion objective (XLUMPlanFL N, NA 1.0, Olympus) and a piezoelectric objective positioner (Physik Instrumente), and it was operated using ScanImage 3.81 acquisition software (Vidrio Technologies). Next, a 17 × 17 grid of voxels (~7 μm square) was defined for every sixth section. Those voxels that lay within the convex hull of antennal lobe ReaChR:mCitrine expression in each slice were then designated for photostimulation. Because the size and orientation of the antennal lobe can vary from fly to fly, the number of photostimulated voxels varied from ~900 to ~1400. The laser was then re-tuned to 1040 nm for photostimulation. Total laser power at the position of the brain was 3.0 mW. This laser power elicited a mean PN firing rate of 15 spikes/sec (averaged over 33 PNs, Table S1); this is within the physiological range of odor-evoked firing rates in PNs, although it lies near the low end of that range (Bhandawat et al., 2007; Olsen et al., 2010). Laser power was monitored daily and laser output was adjusted as needed to achieve this target value. Each recording was divided into trials, with each trial corresponding to a single voxel. Voxels were stimulated in a random order. Each trial comprised a 250-ms baseline period, followed by a 500-ms photostimulation period, and finally a 50-ms post-stimulus period. The photostimulation pattern consisted of 30 repetitions of a square raster scan pattern within each voxel for a total duration of 500 msec. An intertrial interval of ~800 msec provided time for MATLAB to store the recorded voltage trace to disk, load the voxel location for the next trial, and move the piezo-driven microscope objective to the new imaging plane (if necessary). Because of the large number of voxels needed to span the antennal lobe, and because each whole-cell recording had a limited duration, we typically only had the opportunity to stimulate each voxel once, but in some recordings we had enough time in the recording to stimulate some or all voxels twice. When voxels were stimulated twice, the resulting two voltage responses were averaged prior to further data analysis. In these cases, we generally found that the first and second responses were similar (Figure S4). In 8 out of 110 LHN recordings, the recording was lost before all voxels were stimulated, but > 50% of all voxels were nonetheless stimulated, and so we included these recordings in our dataset. Because each glomerulus contains many voxels, and voxels were visited in random order, almost all glomeruli were still typically stimulated in these experiments, but a few glomeruli were missed.

Stimulation of each voxel was targeted to a single z-plane (7 × 7 μm in X-Y), but the z-extent of the excitation volume extended above and below that plane. We quantified this effect in a subset (n = 14) of our PN recordings. Considering just those voxels directly above, within, or below the glomerulus innervated by the recorded PN (identified by filling the PN with Alexa Fluor 568), we compared the number of spikes elicited by photostimulation to the z-distance from the filled glomerular boundary. This analysis revealed that out-of-plane excitation (> 15% of within-plane excitation) extended 1 μm below the focal plane and 6 μm above the focal plane. Thus each voxel corresponds to a volume of excitation of approximately 7 × 7 × 8 μm.

Over the course of the recording session, the position of the brain sometimes shifted by a few μm. In order to ensure a precise spatial alignment of voxels relative to glomerular positions, we periodically paused the sequence of voxel stimulation to check this alignment. The full set of voxels was split into 4 blocks. After completing each block, we imaged ReaChR:mCitrine emission within a fiduciary optical slice of the antennal lobe (at 940 nm) and we adjusted the remaining voxel positions (if needed) to compensate for any shift in brain position. If the brain had moved more than 5 μm in any dimension, we discarded the data acquired in the prior block of recording trials and repeated that block.

### Odor delivery

For *in vivo* LHN recordings (Figures 3 and 8), an air stream (200 ml/min) was passed through activated carbon and directed at the fly through a carrier tube. A separate air stream of 5–30 ml/min was directed under the control of a solenoid valve into the headspace of a

clean 1 mL vial (Thermo Scientific, National C4011-5W) containing 200  $\mu$ l of a solution of odor and paraffin oil or paraffin oil alone. The odor stream joined the carrier stream 11 cm from the end of the tube. Odor pulses were delivered for 1 s, with interpulse intervals of 30 s. Paraffin oil was stripped of low-molecular weight volatiles by storing it under negative pressure for at least 4 weeks prior to use. A flow rate of 12 ml/min was used for hexanoic acid delivery and 30 ml/min for methyl laurate delivery. A flow rate of 5 ml/min was used for all other odors. The higher flow rates were required to evoke responses to hexanoic acid and methyl laurate. Because higher flow rates can lead to stronger paraffin oil responses, the flow rates for control trials (using paraffin oil only) were matched to the flow rates of each odor. Thus, the LHN and PN responses summarized in [Figures 8B](#) and [8C](#) are odor responses from which matched flow-rate paraffin oil responses have been subtracted.

### Calcium imaging of odor-evoked activity in PNs

The PN calcium imaging experiments in [Figure 8B](#) were performed as previously described ([Hong and Wilson, 2015](#)). External saline and odor delivery parameters were identical to *in vivo* LHN electrophysiological recordings. The antennal lobe was imaged from the dorsal side. Two-photon fluorescence of GCaMP6f in PN dendrites was excited with 925 nm light and collected with the same custom-built 2-photon laser scanning microscope and ScanImage 3.7 software used for connectivity mapping experiments. A single imaging trial consisted of 150 frames acquired at a resolution of 128  $\times$  128 pixels and a frame rate of 6.73 Hz. Odor was delivered for 1 s. Multiple Z-planes were imaged sequentially to cover the majority of glomeruli. Glomeruli were identified and masked based on a published atlas ([Couto et al., 2005](#)).

### *In situ* neuropil staining

To identify glomeruli at the end of each connectivity-mapping experiment, we stained the neuropil *in situ*. After stimulating all voxels, we added 10  $\mu$ L of 116  $\mu$ M  $\alpha$ -bungarotoxin conjugated to Alexa Fluor 488 to the saline in the recording chamber (with superfusion turned off) and incubated the brain for 30 min to stain the synapse-rich regions of neuropil. The fluorescent  $\alpha$ -bungarotoxin conjugate was then washed out with 5 minutes of external saline superfusion. After realigning voxel location to glomerular position using the ReaChR:mCitrine signal (imaged at 940 nm), we then imaged the entire antennal lobe at high resolution (at 775 nm). This image was used to identify the boundaries of each glomerulus, and thereby assign voxels to glomeruli post hoc. In PN recordings ([Figure 1](#)), we also imaged the PN's dendrite (filled with Alexa Fluor 568 via the patch pipette internal, imaged at 775 nm) to determine the identity of the PN's home glomerulus.

## IMMUNOHISTOCHEMISTRY AND ANATOMY

To determine the morphology of each recorded LHN, the brain was fixed in 4% formaldehyde, washed, blocked with 5% normal goat serum, and incubated with mouse anti-Bruchpilot antibody (Developmental Studies Hybridoma Bank, nc82 s, 1:50 v/v dilution in blocking solution), then washed again and incubated with goat anti-mouse Alexa Fluor 633 secondary antibody, along with streptavidin Alexa Fluor 568 (1:250 and 1:1000 in blocking solution). Brains were mounted in Vectashield (Vector Laboratories) and imaged with an Olympus FV1000 confocal microscope.

Biocytin fills were visible in confocal images for 94 of 110 LHN recordings. Each of these morphologies were traced by hand using the Simple Neurite Tracer plugin ([Longair et al., 2011](#)) in Fiji ([Schindelin et al., 2012](#)). The corresponding nc82 neuropil stain was then non-rigidly registered to the JFRC2 template brain ([Jefferis, 2014; Jenett et al., 2012](#)) using the Computational Morphometry Toolkit ([NITRC.org](#)). Registration was successful for 89 of the 94 brains with traced LHNs. Subsequent anatomical analysis was performed using the NeuroAnatomy Toolbox ([Jefferis and Manton, 2017](#)). Each traced neuron was registered using the parameters determined from the corresponding nc82 stain. Neurons in the right brain hemisphere were mirrored to the left hemisphere to facilitate comparison. Finally, all neurons were smoothed with a 2  $\mu$ m Gaussian kernel. Morphological similarity was assessed with NBLAST ([Costa et al., 2016](#)) using the function “nblast\_allbyall” in the NeuroAnatomy Toolbox ([Jefferis and Manton, 2017](#)). The NBLAST similarity scores used for analysis were the mean of “forward” and “reverse” scores. LHNs were then hierarchically clustered on pairwise NBLAST scores using Ward's method. LHNs were then grouped into types using a linkage distance of 0.65. The z-projections of single exemplars of each LHN type are provided in [Figure S6](#) and .swc files for all 89 traced and registered LHNs are provided in [Data S1](#).

Automatic morphology classification was possible for the 89 cells which were successfully dye-filled, traced, and registered to a template brain. These cells were classified into 37 types; two types were then manually split because of morphological differences (which were just below the automatic threshold) that correlated with connectivity differences, yielding 39 types in total ([Figure S6](#)). For 11 additional LHNs, we had qualitative morphology data, but template registration failed ( $n = 5$ ) or the dye-fill was not bright enough to confidently trace the cell's full morphology ( $n = 6$ ). We assigned these 11 cells to one of the 39 existing types, because each one qualitatively resembled one of those types. Finally, we used connectivity information ([Figure 4C](#)) to classify the remaining 10 LHNs, where there was no visible dye-fill. For each of these cells, we were able to find a well-filled cell recorded in the same Gal4 line whose connectivity pattern was a reasonable match. We used this information to provisionally assign each of these 10 cells to a type.

The nomenclature we used for LHN types was designed to be simple and pronounceable: cells that were mainly local to the lateral horn were called “local,” whereas cells that had extensive neurites beyond the lateral horn were named according to the predominant regions containing those neurites (M = medial regions, i.e., SMP and/or crepine; L = lateral regions, i.e., SIP and/or SLP; V = ventral

regions, i.e., AVLPL and/or PVLPL; C = contralateral regions). The following types in our study resemble LHN types that have been described elsewhere: L12 (called NP6099 by [Fişek and Wilson, 2014](#)), ML8 (called PD2b1 by [Dolan et al., 2017](#)), ML9 (called Mz671 by [Fişek and Wilson, 2014](#) and PD2a1 by [Dolan et al., 2017](#)), and ML2 (cell 121208-1 within the category called aSP-g by [Kohl et al., 2013](#), i.e., the rightmost female LHN in [Figure 2B](#) of that study).

Brain regions were identified based on established definitions ([Ito et al., 2014](#)) and the corresponding boundaries we used were provided with the JFRC2 template brain ([Jenett et al., 2012](#)). Brain region abbreviations used in [Figure 4B](#) are as follows: SLP = superior lateral protocerebrum; SIP = superior intermediate protocerebrum; SMP = superior medial protocerebrum; CRE = crepine; AVLPL = anterior ventral lateral protocerebrum; PVLPL = posterior ventral lateral protocerebrum; PLP = posterior lateral protocerebrum; MBCA = mushroom body calyx; SCL = superior clamp; LH = lateral horn.

It should be noted that we do not know the locations of pre- and postsynaptic sites in the LHNs we sampled. Given that almost all were found to receive antennal lobe PN input (probably monosynaptic input), we can conclude that they have postsynaptic sites in the lateral horn. Whether they are also presynaptic in the lateral horn is not known. Their neurites outside the lateral horn may contain pre- and/or postsynaptic sites. [Liang et al. \(2013\)](#) have shown that the LHNs we call type V3 have presynaptic sites outside the lateral horn.

## QUANTIFICATION AND STATISTICAL ANALYSIS

### Assessing errors in PN recordings and identifying glomeruli connected to LHNs

For PN recordings, we scored voxels as significant if they evoked at least one 1 spike, and non-significant if they evoked 0 spikes. PNs almost never spiked during the pre-stimulus period of any trial (0.07% of all trials), and so virtually all spikes must be due to photostimulation. PN spikes were detected using custom-written MATLAB routines, with settings that were adjusted as needed for each PN. All trials were inspected visually to ensure that all spikes were detected.

For LHN recordings, we scored voxels as significant if the LHN voltage response exceeded a threshold defined by the LHN's pre-stimulus voltage fluctuations. This threshold was determined separately for each trial. To begin, each trial was divided into 10 msec bins. For each trial, a distribution of baseline activity was constructed using that trial's 250-msec pre-stimulus period, plus the 250-msec pre-stimulus period for the preceding trial, plus the 250-msec pre-stimulus period for the subsequent trial (25+25+25 bins), yielding 75 bins of baseline activity for each trial. This procedure allowed for good sampling of baseline voltage, while staying robust to slow fluctuations in baseline voltage over the course of the experiment. We deemed a voxel as significant if at least 5 consecutive bins during a 400-msec window starting 100 msec after stimulus onset were at least 4 standard deviations above the mean of the baseline distribution.

For both PN recordings and LHN recordings, we scored a glomerulus as a "hit" if two criteria were satisfied. First, at least 25% of all voxels with centers within the boundary of the glomerulus needed to be significant. Second, at least two significant voxels needed to be adjacent. We determined these criteria on the basis of our PN recordings so as to balance the number of false positives and false negatives per experiment. These criteria were then applied identically to PN and LHN recordings. Glomeruli were identified by comparing the neuropil image with reference atlases ([Couto et al., 2005](#); [Grabe et al., 2015](#); [Laissue et al., 1999](#)). It is worth noting that we obtained positive evidence for the efficacy of stimulation for almost every ReaChR-expressing glomerulus: a total of 16 glomeruli were validated directly in PN recordings, and a further 21 glomeruli were validated indirectly by observing an LHN response to that glomerulus.

When false positives occurred in our PN recordings (given the two criteria described above), they most often corresponded to a glomerulus that was immediately adjacent to the PN's home glomerulus. In these cases, the response appeared to "bleed through" from the PN's home glomerulus. To be precise: significant voxels were often skewed toward the edge of the false glomerulus that bordered the true (home) glomerulus. This was in clear contrast to the typical true hit, where the center of mass of significant voxels was well-aligned with the glomerular center. We encountered 8 glomeruli whose responses were clearly due to bleed through in our PN recordings and 87 glomeruli with bleed through in our LHN recordings. We manually removed all these glomeruli from the list of glomerular hits for the corresponding recordings, using identical criteria for visually assessing bleed through in the PN data and LHN data ([Figure S2](#)).

False negatives in our PN recordings also tended to have a characteristic spatial pattern. These were cases where voxels at the glomerular center evoked a PN spiking response, but yet < 25% of total voxels in the glomerulus evoked a response. In our LHN recordings, we occasionally observed an analogous phenomenon (cases where clear EPSPs were evoked by stimulating voxels at the glomerular center, but yet < 25% of total voxels in the glomerulus evoked EPSPs). We encountered 3 glomeruli with "isolated core responses" in our PN data and 21 glomeruli in our LHN data. We manually added all these glomeruli to our list of glomerular hits for the corresponding recordings, using identical criteria for visually assessing "isolated core responses" in the PN data and LHN data ([Figure S2](#)).

Hit rates for PN experiments shown in [Figure 1F](#) and quoted in the text (percentage of PN recordings where home glomerulus was not hit = 3%, percentage of glomeruli identified as false hits in PN recordings = 0.2%) were computed after "bleed through" glomeruli were removed and "isolated core" glomeruli were added.

### Quantifying glomerulus-LHN connection weights

After glomerular hits and misses were scored in the LHN data, the weight of each hit was computed. Weight was defined as the mean LHN voltage change during the stimulus period (relative to the baseline period), averaged across all significant voxels in

that glomerulus. The voltage during the stimulus period was computed over a window beginning 100 msec after stimulus onset and ending at stimulus offset; this 100-ms delay accounted for typical latencies between the onset of glomerular stimulation and the onset of PN spiking. The baseline voltage was assessed during the entire 250 msec baseline window.

### Analyzing correlations between LHNs or glomeruli

In every case where we report correlation values, this corresponds to a Pearson rank correlation coefficient. Agglomerative hierarchical clustering was performed on correlation distances to sort glomeruli in [Figure 5D](#) using an average distance algorithm. Clustering was performed using the `pdist` and `linkage` functions in the MATLAB Statistics and Machine Learning Toolbox. The simulation in [Figure 5B](#) was performed by randomly permuting the glomerulus identities of connections to each LHN independently. This maintains the number of connections to each LHN, as well as the magnitudes of all the connections to each LHN. The simulation in [Figure 5C](#) was performed by randomly permuting the LHN identities of connections from each glomerulus independently. This maintains the number of connections from each glomerulus, as well as the magnitudes of all the connections from each glomerulus. We omitted the 3 LHN types with particularly broad connectivity (local1, local3, and ML4) from [Figure 5](#). If we included them, then the differences shown in [Figures 5B](#) and [5C](#) became larger (and more significant); meanwhile, the correlations in [Figure 5D](#) increased and became more uniform across the matrix. The correlation in [Figure 5G](#) is still significant, and the correlation in [Figure 5H](#) is just short of significant.

### Identifying significantly convergent pairs of glomeruli

The significantly convergent pairs of glomeruli reported in [Figure 6](#) were identified as follows. First, we omitted the 3 broadly connected LHN types (local1, local3, and ML), and we treated excitatory and inhibitory inputs from VA1v as inputs from two separate glomeruli (VA1v-excitation and VA1v-inhibition); the same convention was used for excitatory and inhibitory inputs from DA1. We then binarized the connectivity matrix from [Figure 4C](#). For each pair of glomeruli, the number of recorded LHNs with convergent connections was counted. These counts were then repeated after randomly permuting the LHN labels for each glomerulus independently. This maintains the number of connections to each LHN, but destroys any correlations between glomeruli. We performed 50,000 random permutations to generate a null distribution of convergence counts for all pairs of glomeruli. Significant convergences were detected with a false discovery rate of 0.05 using the Benjamini-Hochberg procedure to control for multiple comparisons.

### Predicting connectivity from anatomy

PN-PN axon similarities ([Figure 7B](#)) were computed with NBLAST ([Costa et al., 2016](#)) using the function “`nblast_allbyall`” in the NeuroAnatomy Toolbox ([Jefferis and Manton, 2017](#)). The NBLAST similarity scores used for analysis were the mean of “forward” and “reverse” scores for pairs of previously published PN axon morphologies ([Chiang et al., 2011](#); [Grosjean et al., 2011](#); [Jefferis et al., 2007](#); [Wong et al., 2002](#); [Yu et al., 2010](#)). The analysis included only the portion of each PN’s axon that was within the boundaries of the lateral horn neuropil, as defined by the JFRC2 template brain. In [Figure 7B](#), we omitted the 3 LHN types with particularly broad connectivity (local1, local3, and ML4), if these LHN types were included, the correlation became stronger. PN-LHN appositions ([Figures 7C](#) and [7D](#)) were measured as the number of potential synapses ([Stepanyants and Chklovskii, 2005](#)) with an approach distance of 1  $\mu\text{m}$  and a Gaussian smoothing kernel of 2.5  $\mu\text{m}$ .

## DATA AND SOFTWARE AVAILABILITY

Raw measurements of PN firing rates evoked by glomerular photostimulation ([Figure 1](#)) and LHN responses to glomerular stimulation ([Figure 4C](#)) are provided in [Tables S1](#) and [S2](#). Skeletonized 3-D morphologies of all digitized LHNs are provided as `.swc` files in [Data S1](#).